

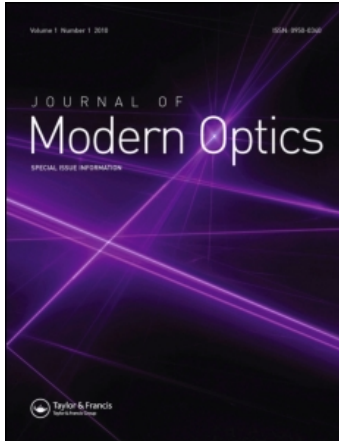
This article was downloaded by: [Imperial College London]

On: 16 June 2010

Access details: Access Details: [subscription number 918057602]

Publisher Taylor & Francis

Informa Ltd Registered in England and Wales Registered Number: 1072954 Registered office: Mortimer House, 37-41 Mortimer Street, London W1T 3JH, UK



## Journal of Modern Optics

Publication details, including instructions for authors and subscription information:

<http://www.informaworld.com/smpp/title~content=t713191304>

### Ultra-fast dynamic imaging: an overview of current techniques, their capabilities and future prospects

C. Altucci<sup>a</sup>; R. Velotta<sup>a</sup>; J. P. Marangos<sup>b</sup>

<sup>a</sup> CNISM and Dipartimento di Scienze Fisiche, University of Naples 'Federico II', Italy <sup>b</sup> Blackett Laboratory, Imperial College London, London SW7 2AZ, UK

First published on: 16 June 2010

**To cite this Article** Altucci, C. , Velotta, R. and Marangos, J. P.(2010) 'Ultra-fast dynamic imaging: an overview of current techniques, their capabilities and future prospects', Journal of Modern Optics,, First published on: 16 June 2010 (iFirst)

**To link to this Article:** DOI: 10.1080/09500340.2010.493621

**URL:** <http://dx.doi.org/10.1080/09500340.2010.493621>

PLEASE SCROLL DOWN FOR ARTICLE

Full terms and conditions of use: <http://www.informaworld.com/terms-and-conditions-of-access.pdf>

This article may be used for research, teaching and private study purposes. Any substantial or systematic reproduction, re-distribution, re-selling, loan or sub-licensing, systematic supply or distribution in any form to anyone is expressly forbidden.

The publisher does not give any warranty express or implied or make any representation that the contents will be complete or accurate or up to date. The accuracy of any instructions, formulae and drug doses should be independently verified with primary sources. The publisher shall not be liable for any loss, actions, claims, proceedings, demand or costs or damages whatsoever or howsoever caused arising directly or indirectly in connection with or arising out of the use of this material.

## TOPICAL REVIEW

### Ultra-fast dynamic imaging: an overview of current techniques, their capabilities and future prospects

C. Altucci<sup>a</sup>, R. Velotta<sup>a</sup> and J.P. Marangos<sup>b\*</sup>

<sup>a</sup>CNISM and Dipartimento di Scienze Fisiche, University of Naples 'Federico II', Via Cintia 26 – Napoli, Italy;

<sup>b</sup>Blackett Laboratory, Imperial College London, Prince Consort Road, South Kensington, London SW7 2AZ, UK

(Received 29 January 2010; final version received 4 May 2010)

In this review we attempt to sketch an overview of the various methods currently being used or under development to enable ultra-fast dynamic imaging of matter. We concentrate on those techniques which combine atomic scale spatial resolution and femtosecond or even sub-femtosecond temporal resolution. In part this review was inspired and informed by the material presented at the 'Ultrafast Dynamic Imaging II' workshop held in Ischia, Italy in April 2009, but we also have drawn on a wider background of material especially when discussing the emerging laser-based methods.

**Keywords:** molecular imaging; ultra-fast processes; ultrashort light pulses; femtosecond dynamics; attosecond physics

#### 1. Introduction

The measurement of the structure and dynamics of matter undergoing the processes of importance in physics, chemistry and biology is the goal of ultra-fast dynamic imaging methods. This goal is of immense importance in the future development of many areas of science and technology as it is often essential to have full information on structural dynamics before a process can be understood and controlled. In material and condensed matter science, chemistry and structural biology, for many decades Ångstrom scale spatial resolution has been achieved using methods such as X-ray diffraction, electron microscopy and X-ray spectroscopy. There is constant pressure to extend our understanding in not only determining static structures but in following the changes that these structures undergo. As a consequence methods of measuring structures with increased temporal resolution, toward the 10 fs regime, are now being sought [1,2], increasing demands for new light sources such as free electron lasers (FELs) [3] and improved methods, e.g. ultra-fast electron diffraction (UED) [4]. In recent years ultra-fast science has made rapid advances towards making measurements of dynamics into the 100 attosecond (as) region [5] even to the few tens of attosecond limit [6] using laser-based techniques. Accompanying this has been a desire to capture the accompanying structural information, and some laser-based techniques are beginning to take steps to do this [7,8].

We can see a clear trend in the scientific requirements to measure matter simultaneously with high temporal and spatial resolution; the need for femtosecond to sub-femtosecond temporal resolution and Ångstrom to sub-Ångstrom spatial resolution is now being demanded and actively pursued. Longer time-scales and larger spatial scales are clearly of great importance too, but here we concentrate on the technologically most challenging, and arguably the scientifically most fundamental, goal of ultra-fast dynamic imaging to the femtosecond/Ångstrom scale. It turns out we have available a range of techniques spanning, for example, laser-based, X-ray based, electron beam based methods and the convergence of these towards the common goal just stated is both challenging and very exciting to scientists active in the field.

There is a danger, however, that the practitioners of each method will appreciate only their own chosen technique and methods and not have a clear view of the broader picture due to the usual barriers of jargon and unfamiliarity. We argue that this is a pity, since we are all driven by curiosity about common scientific goals and wish to understand our colleagues interesting work, and because it is so often found that in appreciating the concepts and methods of another field that we can gain new insights and make advances in our own area. It is thus the intention of this review to attempt, in a modest way, to collect together the major techniques of ultra-fast dynamic imaging and to

---

\*Corresponding author. Email: j.marangos@imperial.ac.uk

briefly explain the underlying concepts and principles of the methods. We aim to be concise and to make this overview readable and accessible. In doing so we will inevitably not cover to everybody's complete satisfaction the full literature, nuances and technical details of each field and must recommend you consult more specialist works to find these (we attempt to point out suitable references where appropriate). A special emphasis is placed upon recently implemented laser-based methods that are offering attosecond domain temporal resolution. The literature is too extensive to review fully so only samples of the work in a given area will be cited. It is therefore very much in the style of a tutorial review aimed squarely at the non-specialist, new researchers just beginning and more experienced scientists looking for an elementary introduction to other methods of ultra-fast dynamic imaging.

### 1.1. Why do we need to measure ultra-fast structural dynamics?

Prior to embarking on our overview of the measurement concepts behind a sample of techniques we would like to ponder why the femtosecond/Ångstrom regime for ultra-fast dynamic imaging is so fundamental. In essence this is because it is the natural spatial and temporal scale for the atomic scale evolution of matter, whether that matter is an isolated small molecule a large molecule in solution or an extended sample of crystalline or amorphous condensed matter. In Figure 1 we present some of the relevant ranges of

time and spatial scales important to a wide class of physical situation.

In particular chemical dynamics and dynamics in the condensed phase span a large range of scales of interest in space and time. There is a great deal of interest, for example, in the large scale structural change of large biomolecules, such as protein folding, which occurs on the picosecond to microsecond timescale. But chemical changes can also occur on much faster timescales and often the key events occurring in say a localised reaction centre, embedded within a much larger complex, takes place in a 100 fs or less. This is because the motion of the atomic nuclei that determines a chemical change takes place on timescales of down to 10 fs or so. The fastest chemical timescales are not much faster than the vibrational period of a proton which when bonded to a carbon atom is around 12 fs, which is about the fastest that nuclei are usually thought to move. This said still faster dynamics associated with electron motion are currently the target of the field of attoscience. Partly this is because understanding the time domain behaviour of correlated electron dynamics in matter is a fundamental problem in physics. Moreover, electron dynamics can play a vital role as the first stage in the ultra-fast events involving the motion of atomic nuclei that occur on a longer timescale, e.g. in chemical dynamics or phase changes within condensed matter. Additionally if for instance we wish to control the system using an external light field that couples primarily to the electrons, we need tools that can measure both electronic and nuclear structure and dynamics.

Capturing the structural dynamics associated with atomic motion within matter thus requires methods that can access Ångstrom spatial resolution with a time resolution in the femtosecond domain. Further to determine the electronic motion and to follow how the spatial properties of the electronic state vary in time (to follow the evolution of the electronic wavefunction) requires Ångstrom spatial resolution and attosecond time domain information. We are starting to have the techniques to address both these goals and such measurements have now been made in a few sample cases. There remains a long way to go before 'universal' methods with attosecond resolution applicable to all systems of potential interest are available but we do now have a well-defined direction of travel towards the highest resolution ultra-fast dynamic imaging through the various techniques we are about to review.

What drives the field forward is the great importance of the goal. There are a huge range of phenomena in science for which we have little or no knowledge of the relevant structural dynamics. If we can gain such knowledge not only will we have a detailed understanding of the mechanisms of myriad phenomena, but

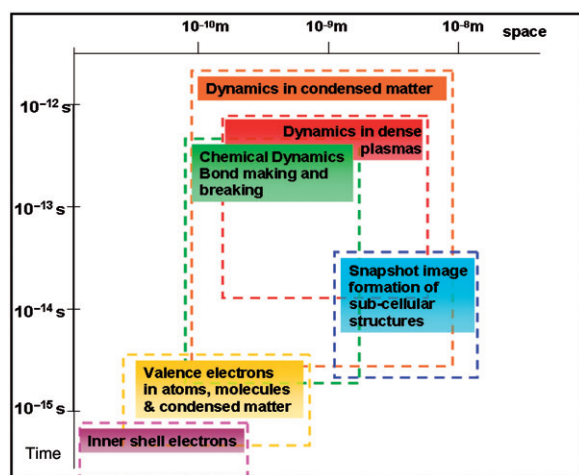


Figure 1. Spatial and temporal scales relevant to key areas of physical and chemical sciences. From 'NLS Project: Science Case and Outline Facility Design' STFC, July 2009. (The colour version of this figure is included in the online version of the journal.)

we will also have a powerful tool for controlling the material world at the quantum scale. We might even claim that whilst establishing the static structures of matter was one of the great technical achievements of twentieth century science a key challenge for the twenty-first century is to establish the structural dynamics.

### 1.2. Towards femtosecond resolved structural dynamics

Structural dynamics demands structural information at the Ångstrom scale. Many laser-based time-resolved spectroscopy methods do not give this spatial resolution even though they allow us to measure the instantaneous state the system is in (electronic or vibrational) with femtosecond resolution. It is true that in simple systems we may have the detailed knowledge of potential energy surfaces (through spectroscopy) requisite to deduce the accompanying structural dynamics. Once we consider more complex molecules or solids where many multi-dimensional potential energy surfaces, and intersections of these surfaces, may play a role, such an approach can rapidly be reduced to mere guess work. Thus, we need a way to directly measure the position of atoms or the shape of an electronic wavefunction with Ångstrom spatial resolution at the requisite temporal resolution. As much as possible we need methods that require no a priori theoretical knowledge of the system being measured and are thus amenable to robust reconstruction of the instantaneous structure. The basic measurement tools available to provide this information are either electromagnetic fields (photons) or particles, with sufficiently short wavelengths to resolve the structure.

In practice, of all the potential candidate probes for ultra-fast dynamic imaging the only two that are so far used are X-rays and electrons. To obtain a resolution of 1 Å from a diffraction measurement requires a comparable or shorter wavelength. Thus, for X-rays we require photons with an energy of 12 keV to achieve a 1 Å wavelength for the electromagnetic field (although significantly lower energy X-ray photons are still widely used for X-ray diffraction measurements at lower resolution). For an electron to have a 1 Å de Broglie wavelength the kinetic energy must be >150 eV, i.e. for high spatial resolution much lower electron energies than photon energies are needed. The use of electrons as the structural probe underpins the X-ray absorption [2] and HHG (high harmonic generation) imaging techniques covered [9], and also the time-resolved electron diffraction and electron microscopy methods. Indeed often X-rays and electrons both

play a role in the measurement, so for instance in X-ray absorption measurements (e.g. EXAFS) [2] the choice of the X-ray wavelength around an absorption edge sets the species sensitivity and through this defines the sites within the matter that will be probed and the liberated photoelectrons provide the spatial resolution of the measurement.

It may be argued that some of the laser-based techniques of femtosecond and attosecond science use a different principle. So for instance information on the instantaneous wavefunction can be obtained by using spatially resolved laser tunnel ionisation methods [10], although here again the electron is implicated in the tunnelling process that constitutes the measurement. In recent time-resolved photoelectron spectroscopy studies [11] the measurement of the outgoing electron angular distribution can be used to deduce valuable structural information, and variants of this using attosecond pulse trains are seeking to fully reconstruct photo-electron wavepackets [12] with sub-femtosecond temporal resolution. Here the outgoing electron wave is mapped in momentum space and thus retrieved. For Coulomb explosion imaging [13,14] detection of the charged ionic fragments is used, and here it is true the probe is neither electron nor photon, but the technique is limited to small structures and cannot access the spatial properties of the electronic wavefunction. Attosecond probing using the isolated attosecond domain XUV pulses obtained from HHG has been used to measure the time dependence of photoionisation in atoms [15,16] and surfaces [17] but does not provide direct spatial information as the HHG radiation is typically only ~100 eV corresponding to a wavelength >10 nm. Nevertheless, the *in situ* measurements associated with HHG imaging of molecules employ the spatial resolution of the laser driven recollision electrons (only ~100 eV in energy but with ~1 Å de Broglie wavelength) and so provide measurements with both exceptional temporal and spatial resolution.

In the future it is possible that other particles already used to probe the structural properties of matter such as neutrons, muons and positrons may be utilised for ultra-fast dynamic structural imaging. This can only happen if ultra-fast sources of these particles, or ultra-fast methods using these particles, can be identified and developed, which is not currently the case.

### 1.3. Pump-probe methods

The usual methodology employed in most ultra-fast measurement is the pump-probe approach. Alternatives, such as exciting the sample with a short pump

pulse and watching the subsequent emission in real time using an ultra-fast detector (e.g. a fast diode or a streak camera) are widely used for time resolution down to picoseconds but the absence of efficient detectors for sub-picosecond resolution have largely precluded these techniques in the femtosecond domain. Instead a pump interaction (usually a light pulse) is used to ‘start’ the event and then it is probed after a short delay  $\Delta t$ . This allows us to capture say the structure at a time  $\Delta t$  after the event starts. To build up a full structural dynamics it is necessary to repeat the measurement over the desired range of  $\Delta t$ . As it is not a single shot measurement, and both pump and probe may cause deterioration of the sample, in a given measurement we must carefully consider whether the same sample can be probed multiple times or we need to replace it with a new and identical sample for each measurement. For destructive probe events, such as the strong field laser methods, the latter is invariably the case.

A key step in almost all ultra-fast measurements is to trigger the dynamics to be studied at a precise instant (e.g. the ‘pump’ step in pump–probe methods). This usually requires achieving an appreciable excitation fraction of the sample in the desired channel whilst minimising excitation into other channels. In fact this is a very challenging requirement. Typically we are interested in the evolution of a system following electronic excitation or vibrational excitation (in molecules)/phonon excitation (in solids). The tools usually employed for this are lasers in the IR–visible–UV range where high power (microjoule level or greater), ultrafast (down to  $\sim 10$  fs) pulses, can be generated using a variety of non-linear optical methods to cover the range from 5 to 0.2 eV. Outside of this range light sources of lower power are available, recently much attention has been applied to efficient sources in the far-IR/THz range (0.2–0.001 eV or 500–2.5 THz). For instance pulse durations of  $\sim 1$  ps with microjoule energies can be generated in the THz region using undulators downstream of short wavelength FELs [18]. There are many physical problems where the dynamics is driven purely by thermal/statistical fluctuations in the system, for example, in biological systems such fluctuations are driven at the ambient temperature, and capturing these, processes require an approach to a triggerable ‘thermal fluctuation’. It is reasonable to imagine that THz pulses (6 THz is equivalent in energy to  $kT$  at room temperature) may be a key capability for mimicking the naturally occurring process.

In fact ensuring efficient and specific excitation of the mode of interest presents the experimenter with great challenges possibly as great as the ultra-fast structural probes themselves. Advances in ultra-fast quantum control methods, such as closed loop control

[19,20] may prove of great value in tailoring electromagnetic fields that efficiently perform this function.

A wide class of processes cannot be readily triggered by light at all due to a lack of appropriate optical response. For these it may be possible to use ultra-short pulsed electron beams to trigger electronic excitation in the sample even if an optical trigger is of no help. Such methods are in their infancy when applied to the ultra-fast regime and much work remains to be done.

## 2. Conventional X-ray based methods

### 2.1. X-ray absorption overview

X-ray absorption has proven an immensely useful technique for establishing the structure and electronic state of reaction centres across a vast range of molecules and solids. Because it is primarily a method of local structural determination (in contrast to X-ray and electron diffraction where global structure may be determined) it is especially well suited to isolating the structure of key centres relevant to the functioning of molecules and condensed matter systems. It naturally lends itself to time-resolved extension; although such an extension is not without considerable technical challenge. Often the key initial reaction event in a complex system (e.g. at a chromophore in a biological molecule) happens locally and very quickly (on femtosecond timescales) and is then followed by slower timescale changes on a larger spatial scale. Thus, X-ray absorption is especially suitable for capturing the essential initial ultra-fast component of structural dynamics in a gas, liquid or solid phase system. Crucially the technique is equally applicable to crystalline and non-crystalline solids as well as to molecules in gas and liquid phase.

Various modalities of the technique are available. For absorption signatures it is possible to look at the absorption structure far above the absorption edge ( $>10$  eV) and in this EXAFS (extended X-ray absorption structure) regime local structure is easily extracted as the situation is robustly understood. Closer to the absorption edge in the near edge XANES (X-ray absorption near edge structure) region ( $\sim 10$  eV) the structure may be very rich, and although it is theoretically more challenging to understand, it contains a wealth of information on the local chemical environment, valence electronic structure and local symmetry around the absorbing atom. As an alternative to measure the absorption it is also possible to probe the subsequent photoemission as the vacant core holes are filled as the signal will also be proportional to the photoabsorption cross-section and has the advantage of appearing on a dark background. Alternatively

(at least in the gas phase or at surfaces) the photoelectrons may be directly measured to give complementary information.

In X-ray absorption measurements the X-ray radiation is tuned to the wavelengths around the absorption edge associated with photoionisation from an atomic core state (in the K or L shell) of the target atomic species and absorption of the photon leads to emission of a photoelectron with excess kinetic energy determined by how far the X-rays are tuned above the absorption edge. In the EXAFS regime (extended X-ray absorption fine structure) the photoelectron has kinetic energy in the range 10 to a few 100s eV. Structural information is obtained from the interaction of the outgoing spherical electron wave with neighbouring atoms [21]. The total photo-excitation (photo-absorption) amplitude is the sum of all possible channels including the dominant direct channel and backscattered channels from nearest neighbour, next nearest neighbour atoms etc. Typically in the EXAFS region only a single scattering event makes an appreciable contribution which greatly simplifies the interpretation. Modulation as a function of photon energy (i.e. electron wavevector) of the measured photo-absorption results from interference between channels contributing to the final photo-emission probability (i.e. direct plus backscattered channels) and may be constructive or destructive leading to photon energy dependent peaks and troughs modulating the photo-absorption cross-section by typically a few percent. There is a simple mapping between the electron energy (momentum) at which the maxima and minima occur and the inter-atomic separation between the photon absorbing and backscattering atom.

The theory behind interpreting the EXAFS structure is now very well understood and permits rapid analysis of the structure around the absorbing atom. Consider the measured normalised absorption spectrum  $\chi(E)$  that can be transformed into the normalised absorption spectrum in terms of electron wavevector  $\chi(k)$  through the relation  $k = (2\pi/\hbar)[2m_e(h\nu - E_B)]^{1/2}$ , where  $\nu$  is the X-ray frequency and  $E_B$  is the binding energy (and the other symbols have their usual meaning). For the EXAFS region if we consider an emitting atom surrounded by a group of identical atoms of type  $j$  at a distance  $R_j$  such that there are  $N_j$  of these and each backscatters with an amplitude  $f_j(k)$  and phase shift  $\phi$ , then the quantity  $\chi(k)$  will be:

$$\chi(k) = \sum_j S_0^2 N_j \frac{|f_j(k)|}{k R_j^2} \sin[2kR_j + 2\delta + \phi] C(k) \quad (1)$$

where  $\delta$  is the phase shift for the electron at the parent atom and  $C(k)$  is a factor accounting for the finite range of the electron wave and statistical fluctuations

of the lattice. The key to extracting the structure from the absorption modulation lies in the  $\sum_j \sin[2kR_j + 2\delta + \phi]$  terms. This is somewhat analogous to the ‘structural interference’ signatures recently claimed for molecular HHG.

X-ray absorption near edge (XANES) refers to the structure immediately above an absorption edge extending up to 30 eV or so. This encodes in principle longer range structure (recall the reciprocal relationship between the energy and the spatial scale through the  $kR_j$  factor) and symmetry information as well as additional information on the chemical state of the system. XANES contains information on the molecular structure and also the electronic state. The geometrical arrangement of the atoms in a local cluster around the X-ray absorbing atom is responsible for part of the XANES structure. It is possible to interpret this structure from the lower energy of the electrons, although the fact that multiple scattering is important makes the picture more complex than for the interpretation of EXAFS where higher energy electrons are singly scattered. Absorption features in the 10 eV energy range above the absorption threshold have a physical origin, which is different for different classes of materials e.g. bound valence states or quasi-bound states (so-called shape resonances) in molecules or core excitons in ionic crystals.

To understand the potential for temporal resolution we can consider the effect of the electrons backscattered from the nearest neighbour atoms as the inter-atomic distance is changed. Imagine a hypothetical example where the inter-atomic distance is initially  $r = 1.2 \text{ \AA}$  and an interference from the backscattered wave is expected if the de Broglie wavelength is  $\lambda = 2r = 2.4 \text{ \AA}$ , which corresponds to an electron kinetic energy of around 24 eV (ignoring the phase shift terms). If, however, there are some dynamics and the inter-atomic spacing is reduced to say 1.1 Å then this interference feature will shift to 28.5 eV above the edge. The timescale for the backscattering is itself very fast, even for these relatively low kinetic energy electrons the round trip time of the backscattered electron is only  $\sim 0.15 \text{ fs}$  in the above example so in principle the time resolution limit is in the sub-femtosecond regime (if sufficiently short and well synchronised pump and probe pulses were available). Of course there may be other practical factors (such as temporal walk-off between pump and probe) that limit the temporal resolution.

Recently a method of X-ray spectroscopy has been introduced that utilises the effect upon the observed spectrum of ultra-fast (few femtosecond) Auger decay following the photoexcitation. This Auger ‘clock’ method has recently been implemented in a number of measurements where for instance the few

femtosecond delocalisation of a valence electron excited at an initially localised site within a material has been measured [22]. This is a powerful method for following charge transfer dynamics in matter even down to the sub-femtosecond regime, we will return to it briefly in Section 5.3.

Novel studies on sub-picosecond time-resolved structural changes from X-ray absorption have recently been reported by a number of authors [23,24]. Whilst there are many light sources available, including laser-produced plasmas and synchrotron radiation from storage rings, that access the nanosecond and picosecond range (to resolutions of a few tens of picoseconds), as for any X-ray technique, achieved femtosecond resolution requires additional effort with the light sources. In recent years use of laser-produced plasma emission for studies of melting dynamics have yielded a few picosecond resolution [25].

The sample thickness is of significance in determining the actual temporal resolution. Typically samples of 100  $\mu\text{m}$  to several mm are used and as the refractive index of the optical range pump ( $\sim 1.5$ ) and X-rays ( $\sim 1$ ) are significantly different the pulses travel at different speeds in the medium. It can be seen that in a sample of 100  $\mu\text{m}$  thickness the temporal resolution can be no better than 100 fs. Similar constraints apply to time-resolved X-ray diffraction. This dictates the use of the thinnest possible sample to maintain acceptable temporal resolution.

The current best performance for high temporal resolution X-ray absorption studies come from temporal slicing of synchrotron pulses using a laser (as implemented for instance at Swiss Light Source, Advanced Light Source, and European Synchrotron Radiation Facility) that can produce X-ray pulses of  $\sim 100$  fs duration and although these are at a low repetition rate ( $\sim 1$  kHz set by the laser) and contain far fewer photons than the parent synchrotron pulse (in proportion to the temporal reduction) they have been successfully used for X-ray absorption. These measurements have established the potential of the technique even though there were very weak signals due to the lack of suitably bright short pulse X-ray sources.

An important recent example is a time-resolved XANES measurement and we use this to illustrate the potential and current limitations [26]. The study concerned the ultrafast formation of the lowest quintet state of aqueous iron(II) tris(bipyridine) upon excitation of the singlet metal-to-ligand charge-transfer (1MLCT) state by a femtosecond optical pump. The X-ray probing used X-ray absorption near-edge structure (XANES) of the iron K edge at 7.125 keV. A 100  $\mu\text{m}$  thick free-flowing liquid jet of an aqueous solution of 50 mM  $[\text{FeII}(\text{bpy})_3]^{2+}$  was excited by an intense 400 nm laser pulse (115 fs pulse width,

repetition rate 1 kHz). The tunable femtosecond hard X-ray pulse from the slicing source was used to probe the system in transmission mode at 2 kHz. The flux of the femtosecond X-ray source was about 10 photons per pulse requiring data accumulation times of many hours for the complete measurement. The intensity of a characteristic XANES feature as a function of laser pump/X-ray probe time delay was measured (see Figure 2). It was found that the quintet state was populated in about 150 fs. This result resolved that the population mechanism of quintet states in iron(II)-based complexes was a simple 1MLCT $\rightarrow$ 3MLCT $\rightarrow$ 5T cascade from the initially excited state with the time scale of the 3MLCT $\rightarrow$ 5T relaxation corresponding to the period of the iron–nitrogen stretch vibration.

X-ray FELs have a great deal to offer time-resolved X-ray absorption measurements. FELs can readily reach pulse durations of a few tens of femtoseconds or less, and if seeded can be synchronised to the pump sources to femtosecond accuracy, so that time-resolutions of 20 fs or less look likely to be available [27]. Even more significant than this  $\sim 10$  times improvement in the temporal resolution compared to slicing sources on synchrotrons is the fact that the average electron flux within the pulse duration and required

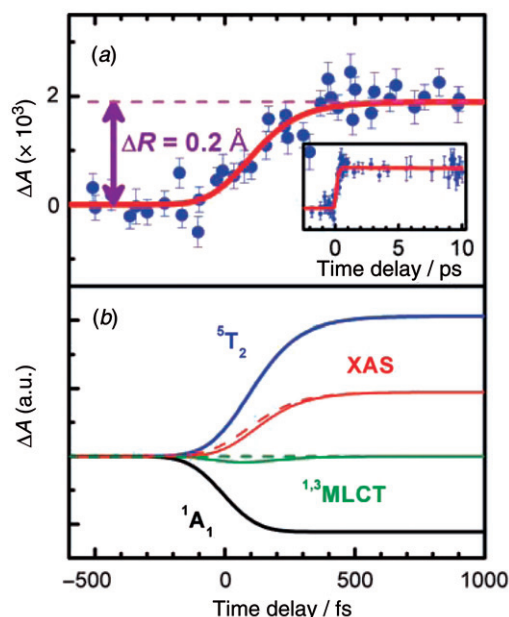


Figure 2. (a) Measured time-dependent differential absorption at the wavelength of the absorption feature corresponding to the transient species (7126 eV). (b) Simulated time dependence of the absorption of three states involved in the fast reaction within the complex (black, green, blue) and the total absorption (red) illustrating the agreement with the measurement. Reproduced with permission from Bressler et al., *Science* **2009**, 323, 489. Copyright (2009) by AAAS. (The colour version of this figure is included in the online version of the journal.)

spectral bandwidth is  $10^4$ – $10^6$  times higher than the brightest synchrotron based source. This high brightness will allow a vast range of time-resolved X-ray spectroscopy measurements to be conducted in solids, gas and liquid phase chemistry and even in dilute samples relevant to biochemistry in living systems.

## 2.2. X-ray scattering

X-ray diffraction from crystals is probably the most famous of all structural methods [28]. It is responsible for the majority of the protein structures so far determined. Notable historic landmarks include the solution of the structure of DNA [29]. It has been just as important in determining the structure of inorganic solids. The theory is too well known to be usefully reviewed here and is available in all textbooks on X-ray diffraction so we will skip any details of this and concentrate instead on time-resolved applications of the technique.

The periodicity of the atomic array in the lattice leads to well-defined Bragg peaks at a scattering angle  $\theta$  satisfying the Bragg condition on the X-ray wavelength  $\lambda$  and an interatomic spacing between two atoms  $i$  and  $j$ ,  $d_{ij}$ :  $\sin \theta = \lambda/d_{ij}$ . Typically the positions and intensities of many thousands of Bragg peaks must be determined to solve a structure for a complex system (like a protein). This requires stable high fluence X-ray sources (synchrotron radiation from electron storage rings have proven an ideal source) and good quality crystals. A global structure of the positions of every atom in a very large system can be determined with an accuracy of a tiny fraction of an Ångström for each atom. The formation of the Bragg peaks results from the highly periodic nature of the crystal structure which ensures efficient scattering into these peaks. For periodic materials the X-ray scattering is efficient due to the coherent addition from a very large number of equivalent scattering atoms. This is important since X-ray elastic scattering is significantly less probable than inelastic scattering. Inelastic scattering causes damage to the sample and it is essential that sufficient scattering occurs before the accumulated damage adversely affects the sample. For materials with only short range order, but lacking long range order, like amorphous solids and liquids, X-ray diffraction is still a powerful probe of local structure. In amorphous matter structural information can still be determined, for instance the distance to nearest neighbour atoms. Powder diffraction and diffraction from polycrystalline samples gives diffraction rings that provide precise information on the local atomic arrangement.

It is in principle straightforward to develop time-resolved extensions (see below). Not all material systems are able to be studied in this way, for instance if the sample is non-periodic in character, and this includes many very important problems for instance in biology. Nevertheless, in two important areas time-resolved crystallographic studies have been performed: time-resolved studies of melting and shock formation in crystalline matter [30–34] and time-resolution of dynamics in some proteins [35,36].

It is far from true that all matter has such regular periodicity. For non-periodic structures the X-ray scattering pattern no longer yields well-defined Bragg peaks or rings, nevertheless if coherent X-rays are used a characteristic scattering pattern still results somewhat akin to the speckle pattern seen from laser illumination of random media. In this way the scattered pattern contains reciprocal-space information from which the object may be imaged. Conventionally this was done using X-ray microscopy to yield a real space image employing X-ray optics, but in practice this method has serious resolution limitations set in part by the technological limits of the optics. Recent advances in analysis of the coherent diffraction images themselves have shown that the ‘phase problem’ can be solved using a new generation of powerful algorithms [37–39]. The trick is to ensure that the object to be imaged is within the X-ray beam and the rest of the field of view contributes no significant scattering signal, this ‘finite support’ constraint then permits the algorithm to efficiently retrieve the phases. This is opening up a new generation of X-ray imaging possibilities based on coherent diffraction imaging (CDI) especially attractive for analysing non-periodic objects that occur widely in nature, e.g. in biological systems. With high brightness X-ray pulses from FELs it is becoming possible to get a sufficiently strong scattered signal to carry out single shot CDI which then opens up the possibility of imaging non-reproducible, non-periodic, objects [40]. Already first time-resolved studies have been carried out on reproducible nanostructures [41].

At the present time the status of time-resolved X-ray diffraction is in a state of flux as the first FEL sources are now available. Already some time-resolved CDI experiments have been carried out at FLASH and it is anticipated that shortly experiments conducted at the newly commissioned LCLS will start to be reported. Soon the first hard X-rays at LCLS will permit the first FEL based time-resolved crystallography. Already a great deal of effort has gone into time-resolved crystallography of materials and proteins using the light sources so far available including synchrotron radiation [42], laser-plasma sources [33] and linac based undulator spontaneous synchrotron radiation [43]. These have been able to show the time

variation of crystal structure following some optical trigger event down to  $\sim 1$  ps temporal resolution.

The first time-resolved structural imaging using CDI from the FLASH FEL operating at 13.5 nm was recently reported [41]. Destruction of a nanostructure initiated by an optical laser pulse which ablates the material was time resolved by taking a series of CDI images using changing time delays [41] as can be seen in Figure 3.

### 2.3. Inelastic X-ray scattering and attosecond resolved electron dynamics

Inelastic X-ray scattering can also be studied and recent results have yielded remarkable findings showing the evolution of electronic states on attosecond timescales with sub- $\text{\AA}$  spatial resolution [44]. In the case of inelastic scattering the scattered X-ray photon has a small energy deficit compared to the incoming X-ray photon with the difference (typically from a few to a few tens of eV) taken up by electronic excitation of the scattering medium. Although the inelastic cross-section is very weak it can still be used to determine the electronic response function of the medium. So for instance in their first measurement of this kind. Abbamonte and co-workers studied the inelastic X-ray scattering from water which is dominated by the response of the electron plasmon in the 2s shell of the oxygen atom. By making precise measurements of the energy and momentum transfer of the inelastically

scattered X-rays the response function  $\chi(\mathbf{k}, \omega)$  was determined. In these spectral domain measurements short X-ray pulses are not required.

The next step is to invert the energy shift and momentum transfer resolved inelastic scattered X-rays via Fourier transformation to give the position–time response function  $\chi(\mathbf{r}, t)$ . The problem is that no phase information is recorded, thus to implement the successful retrieval an additional condition is required. This condition comes naturally from causality (Kramers–Kronig condition) and essentially forces the time direction of the event to be determined as we know that before the incident photon interacted there was no excitation. Applying this aptly named causality-inverted inelastic X-ray scattering method it is possible to generate the charge density variation  $n(\mathbf{r}, t)$  with exceptional temporal and spatial resolution (see Figure 4). The spatial resolution is set by the range of momentum transfers sampled ( $4.95 \text{ \AA}^{-1}$  in the case of water) and the temporal resolution by the range of energy transfers (100 eV in the case of water) so a 41 as temporal and 1.27  $\text{\AA}$  spatial resolution was obtained in the case of water. The raw data must be analytically continued to infinite frequency and the data between sample points interpolated to generate a smooth function to be transformed. The range of the measurement in space and time is set by the sampling frequency whereas the resolutions are set by the total range over which the energy and momentum transfer are measured.

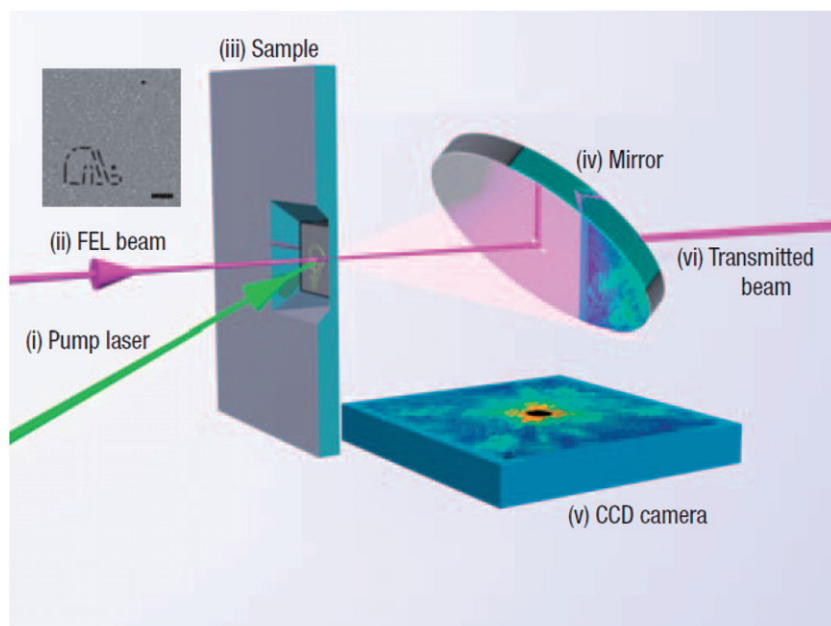


Figure 3. Time-resolved coherent diffraction imaging of laser ablation of nanoscale structures using single pulses from FLASH synchronised to the laser pump pulse. Reproduced with permission from A. Barty et al., *Nat. Photon.* **2008**, 2, 415–419. Copyright (2008) by Nature Publishing Group. (The colour version of this figure is included in the online version of the journal.)

The power of causality inverted IXS was further demonstrated by a study on the alkali halide solid LiF where evidence was sought for the character of the exciton state formed when a photon liberates an electron that remains coupled to the hole [45]. A controversy had existed for many years as to the character of this exciton. On the one hand, the electron may remain localised to the hole on an atomic scale to form a so-called Frankel exciton or on the other hand the electron-hole system may be significantly delocalised to form a Wannier exciton. These two cases lead to very different spatio-temporal behaviour of the charge density with the shape of the disturbance not changing significantly in time in the case of a Frankel exciton. Causality inverted IXS was used to measure the spatio-temporal behaviour of the charge density. To do this the scattering of monochromatised 7.6 keV X-rays from a LiF crystal was measured at the Advanced Photon Source. The exciton centred around  $\sim 14.5$  eV was found to give a rather narrow spectral feature in the scattered energy shift already supporting the view that the exciton was dominantly of local character. The inelastic scattering was studied over an energy shift range from 0 to 100 eV which was sufficient to determine the temporal evolution to  $\sim 20$  as resolution whilst the momentum transfer was measured over a range sufficient to achieve 0.5 Å spatial resolution. The retrieved spatial-temporal structure of the exciton showed that it did not change shape with time, thus confirming the Frankel character.

It is pointed out that the results are really from an average over the whole sample not a single centre.

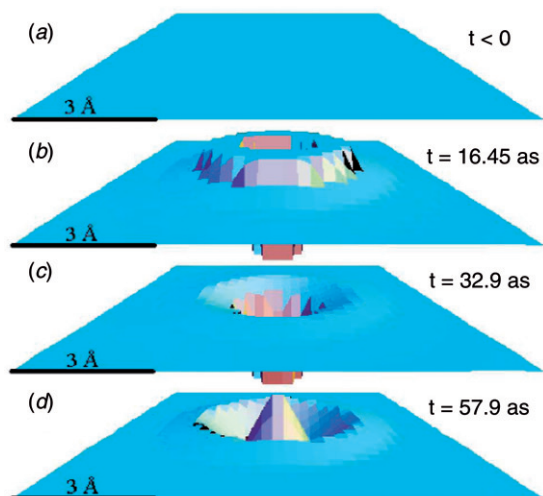


Figure 4. Early behaviour of the electron density disturbance in water arising from a point perturbation (X-ray ionisation). Reproduced with permission from P. Abbamonte et al., *Phys. Rev. Lett.* **2004**, *92*, 237401. Copyright (2004) by the American Physical Society. (The colour version of this figure is included in the online version of the journal.)

This property makes the technique amenable to a system where all inelastic scattering is from the same atomic site (e.g. H<sub>2</sub>O is dominated by the water 2s shell). Extension to other types of system is not obvious although the authors suggest using standing wave approaches to further localise to sites of interest. The method does not require a short pulse light source but rather relies upon the inversion of scattering data from quasi-CW X-rays.

### 3. Electron beam based methods

#### 3.1. Electron diffraction

Electron diffraction phenomena have a long history, indeed it was by observation of diffraction light scattering of electrons from metallic samples that the wavelike nature of the electron was first observed [46,47]. Electrons scattering from a lattice show strong diffraction peaks with angular position determined by the Bragg condition. Electron scattering has been widely used in many areas of science and typically uses electron beams with electron energies in the range keV to 100 keV so the electron wavelength is usually much shorter than the interatomic spacing. Electrons are also extensively used for direct imaging, electron microscopy, where electron optics are used to carry out the function of the lenses in an optical system.

An advantage of electrons (compared to X-rays) is that the electron scattering cross-section is much higher as it is mediated by the Coulomb interaction with both electrons and nuclei. Scattering cross-sections for electrons are typically 4–6 orders of magnitude larger than for X-rays. Electron diffraction is therefore superior to X-ray scattering for examining thin specimens due to the larger cross-sections that allow the study of surface phenomena, the bulk structures of thin foils and membranes, as well as molecular structures of gas phase samples. Moreover, the ratio of inelastic to elastic scattering cross-section for electrons is lower for electrons than for X-rays and the energy deposited into the target per elastic collision is therefore lower for electrons. As a further consequence sample damage presents a less stringent limit. Because very thin samples may be used (down to a few nanometres) any temporal walk-off between electron beam and optical excitation pulse can be minimised.

The major challenge for UED is to deliver an acceptable number of electrons in a pulse short enough to meet the temporal resolution requirements. The strongest limit is imposed by the initial electron momentum spread and the Coulomb interaction between electrons in the pulse (space charge) that cause significant temporal spreading even if only a few thousand electrons are present. The main thrust of

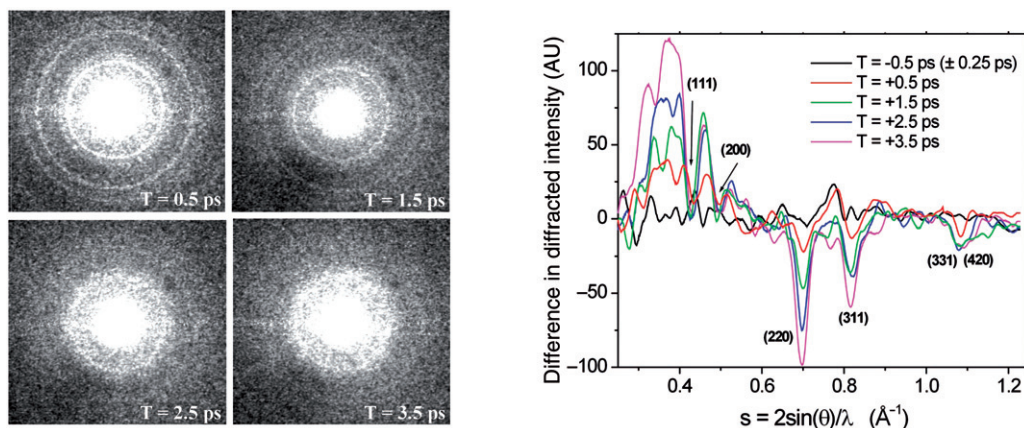


Figure 5. Electron diffraction images of melting of polycrystalline Al (left) with analysed time dependent structure (right). Reproduced with permission from B.J. Siwick et al., *Science* **2003**, 302, 1382. Copyright (2003) by AAAS. (The colour version of this figure is included in the online version of the journal.)

ultra-fast electron diffraction (UED) research is thus to limit the temporal spread by careful design of the electron optics and pulse parameters. An alternative approach to UED is to accelerate the electrons into the relativistic range and so to ameliorate the space charge effect and this has also recently begun to be investigated.

### 3.2. Ultra-fast electron pulses: non-relativistic and relativistic *e*-beams

A number of recent experiments have demonstrated time-resolved electron diffraction. For instance Siwick et al. [4] were recently able to measure the melting of laser heated Al with atomic resolution using a specially designed pulsed electron source. Other measurements of molecular dynamics in the gas phase [48,49] have also been carried out. Earlier measurements were hampered by space charge broadening and reducing the number of electrons in the pulse to reduce that effect leads to loss of resolution in the scattering signal.

To overcome this Siwick et al. designed an optimised pulsed electron source starting with simulation of space-charge-induced pulse broadening [50] to design a photoactivated electron gun that delivered sub-500 fs electron pulses with sufficient number densities for structure determinations with  $\sim 100$  shots [48]. The apparatus comprised the femtosecond laser-driven 30 keV electron source, a sample positioning system an external, lens-coupled, CCD camera to image the diffraction patterns and microchannel plate-phosphor screen detector all mounted in a high-vacuum chamber. As a result they were able to measure the melting dynamics in Al initiated by a 120 fs near-infrared (775 nm) laser pulses, at a  $70 \text{ mJ cm}^{-2}$  fluence, which

was synchronised to the electron source. Diffraction patterns with excellent signal-to-noise were obtained using 150 shots of 600 fs pulses of electrons with  $\sim 6000$  electrons per pulse. The high quality of the data shown in Figure 5 is due to both the large elastic scattering cross-section of electrons and the relatively high efficiency of detection.

An alternative approach that promises to reach sub-100 fs temporal resolutions is to rapidly accelerate the electrons to energies of multiple MeV. The effect of space-charge repulsion on pulse broadening is greatly reduced in the laboratory frame due to Lorentz contraction. Also because the electrons are accelerated so quickly out of the photocathode, where the space-charge broadening is usually highest, the effect on temporal broadening is much reduced. Such a scheme has been implemented in the SLAC laboratory and the ultra-short electron beam was used to record the static structure of an Al film [51]. A single, ultrashort pulse with 5.4 MeV energy impinged on a 160 nm Al film and the diffraction was obtained in the single-shot. The beam pulse duration was 500 fs in these experiments but pulse compression within the rf gun can counter temporal broadening effects, and simulations suggest that a time resolution exceeding 100 fs is possible. A new facility for time-resolved structure determination based on relativistic UED is being set up at the UCLA (Pegasus Project). Conventional UED is performed with electron pulses in the energy range 20–300 keV with  $10^4$ – $10^5$  electrons per pulse whereas it is predicted that relativistic UED will use 3–5 MeV pulses with  $10^7$ – $10^8$  electrons per pulse. The temporal resolution of conventional UED is  $\sim 1$  ps whereas relativistic UED should attain  $< 100$  fs. Nevertheless, in relativistic UED the Bragg scattering angle is exceptionally small (just 0.5 mrad for an internuclear separation of 2 Å)

and so a long distance is required between sample and detector so that this clears the unscattered electron beam as well as very high electron beam quality.

To reach much faster temporal resolution in the sub-femtosecond regime from electron diffraction and microscopy there are a number of proposals based upon using carefully synthesised laser fields to focus electrons in space and time via the ponderomotive force [52,53]. Although these are not yet proven such methods are very promising. As will be explained later there is also much current interest in laser induced electro diffraction as this method has potentially these attributes also.

#### 4. Laser based techniques

Strictly speaking many of the techniques that are to be reviewed next; Coulomb explosion, laser induced electron diffraction, attosecond XUV probes and HHG probing, are all laser based. Nevertheless, the latter two have seen so much recent activity that they will be dealt with in their own separate sections, 5 and 6, respectively.

##### 4.1. Coulomb explosion

Coulomb explosion imaging experiments are based on the detection of multicharged atomic ions arising when molecules are exposed to such intense laser pulses that several electrons are promptly ejected by nonresonant interactions and molecules undergo rapid bond breaking on the repulsive Coulombic potential energy surface of the highly charged states [54]. At zero-order approximation these energy surfaces are governed by the electrostatic Coulomb repulsion of the multicharged atomic ions which are considered as point-like charge. As in general the electron emission can occur over several cycles, the time resolution turns out to be of the order of the pulse duration and, hence, to avoid any significant molecular stretching during multiple ionisation few cycle laser pulses are desirable. This is particularly true when light molecules are studied as in for example the work of Legare et al. [55], in which the authors analysed the explosion of  $D_2O$  and  $SO_2$  at laser intensities in the range  $3\text{--}5 \times 10^{15} \text{ W cm}^{-2}$  with pulse length of 8 and 40 fs, respectively. The gas density was kept low in order to be able to have less than one exploded molecule per laser shot, whereas momentum conservation and the detection of all the ions in coincidence allowed the reconstruction of the molecular structure. In Figure 6 we show the reconstruction of  $D_2O$  obtained by Legare et al. with a pulse length of 8 fs.

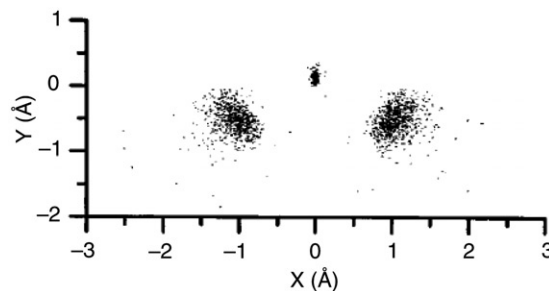


Figure 6. Structure of  $D_2O$  using the 4+ charge states  $D_2O^{4+} \rightarrow D^+ + (O_2)^{++} + D^+$ . The centre of mass is at  $x=0$ ,  $y=0$ , and the  $y$  axis is the bisector of the angle. Reproduced with permission from F. Légaré et al. *Phys. Rev. A* **2005**, *71*, 013415. Copyright (2005) by the American Physical Society.

At such short pulse length a similar result was found also for  $SO_2$ , whereas at longer pulse length (40 fs) the effect of the molecular stretching – leading to the Charge Resonance Enhanced Ionisation [56] – distorted both the images although for  $SO_2$  the effect was less dramatic because of the higher atomic mass.

Previously, Coulomb explosion was analysed by applying the covariance mapping introduced by Frasinski et al. [57]; in this way, the structure of  $CO_2$  and  $SO_2$  was deduced with pulse duration of 150 and 50 fs, respectively (see [56] and references therein). The major limit to the fidelity of the images achieved through Coulomb explosion is the dependence of atomic and molecular ionisation potential on the nuclear coordinates which leads to a distortion of the measured probability density describing the nuclear wavefunction unless the ionisation is not saturated. Thus, laser Coulomb explosion imaging is less suitable for measuring stationary state molecular structures than spectroscopic or thin foil techniques [58]. However, laser Coulomb explosion imaging can be a formidable tool to follow structural changes during photochemical reactions in view of the natural implementation of a pump–probe approach. Hishikawa et al. have demonstrated the visualisation of ultrafast hydrogen migration in deuterated acetylene dication ( $C_2D_2^{2+}$ ) by employing the pump–probe Coulomb explosion imaging with sub-10 fs intense laser pulses (9 fs,  $0.3 \times 10^{15} \text{ W cm}^{-2}$ , 800 nm) according to the scheme depicted in Figure 7(a) [59].

The angle  $\theta_{12}$  between the momenta of the resultant  $D^+$  and  $C^+$  fragment ions,  $p_1(D^+)$  and  $p_2(C^+)$ , is expected to be small due to its linear geometry, whereas large  $\theta_{12}$  values should be observed when the hydrogen migration proceeds towards the vinylidene configuration (see Figure 7(b)). In order to see how the location of the migrating deuterium is mapped to the momentum angle  $\theta_{12}$ , the authors simulated the

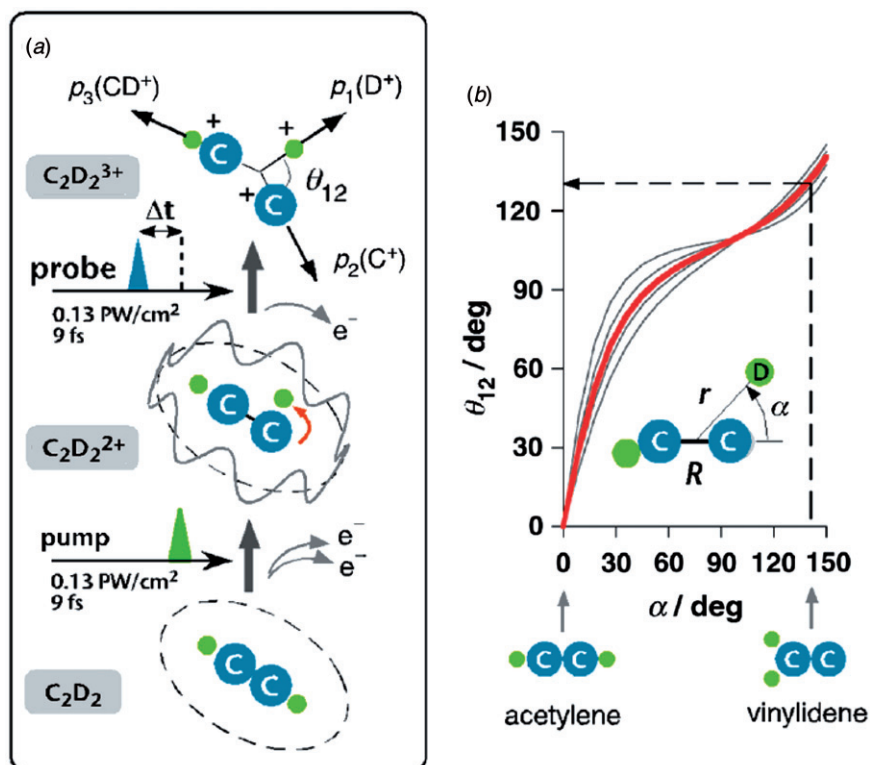


Figure 7. (a) Pump–probe Coulomb explosion imaging employed in [59]. The pump pulse creates  $C_2D_2^{2+}$  and triggers the hydrogen migration. The instantaneous location of migrating deuterium atoms is determined from the momenta of fragment ions,  $D^+$ ,  $C^+$ , and  $CD^+$ , ejected in the Coulomb explosion of  $C_2D_2^{3+}$  induced by the probe pulse. (b) Momentum angle  $\theta_{12}$  as a function of the polar angle  $\alpha$  obtained by the classical simulation of three-body Coulomb explosion (red line) for the structural parameters,  $r = 1.8 \text{ \AA}$  and  $R = 1.34 \text{ \AA}$ , that correspond to the geometry of acetylene dication in the ground state. Results obtained for other radial distances (grey lines),  $r = 1.4, 1.6, 2.0,$  and  $2.5 \text{ \AA}$  (from top to bottom), show that the vinylidene configuration ( $\alpha = 140^\circ$ ) corresponds to the momentum angle of  $\theta_{12} \sim 130^\circ$ , irrespective of the radial distance. Reproduced with permission from A. Hishikawa et al. *Phys. Rev. Lett.* **2007**, *99*, 258302. Copyright (2007) by the American Physical Society. (The colour version of this figure is included in the online version of the journal.)

three-body Coulomb explosion by numerically solving the classical equation of motion, in which each fragment ion is treated as a point charge. The results obtained at different positions ( $r, \alpha$ ) of D in the molecular frame are shown in Figure 7(b). The acetylene ( $\alpha = 0^\circ$ ) and vinylidene ( $\alpha \sim 140^\circ$ ) configurations lead to the Coulomb explosion with different momentum angles,  $\theta_{12} = 0^\circ$  and  $130^\circ$ , respectively. These values are insensitive to the radial coordinate  $r$ , showing that a slight increase in the C–D bond length that may occur in the sub-10 fs probing process [55] causes little effect on the  $q_{12}$  distribution. Thus, from the temporal evolution of the momenta of the fragment ions produced by the three-body explosion,  $C_2D_2^{3+} \rightarrow D^+ + C^+ + CD^+$ , it is shown that the migration proceeds in a recurrent manner: the deuterium atom first shifts from one carbon site to the other in a short time scale ( $\sim 90$  fs) and then migrates back to the original carbon site by 280 fs, in competition with the molecular dissociation.

#### 4.2. Laser recollision electron diffraction

Electron diffraction is one of the most effective techniques for analysing the structure and dynamics of molecules due to the large scattering cross-section between electrons and atoms. At a time resolution level of several hundreds of femtoseconds a successful strategy adopted to trace the temporal changes in the nuclear structure of molecules is the so-called Ultrafast Electron Diffraction dealt with in Section 3 [60], in which ultrashort electron pulses are generated by illuminating a photocathode with a weak laser pulse and accelerated by a static voltage to energies of a few tens of keV. Ultrafast electron diffraction experiments have been performed with picosecond resolution for gas phase experiments [48,61] and (hundreds) femtosecond resolution in solid-state experiments [4,62]. Although attempts are made to increase the time resolution [52,63] space-charge broadening still limits the time resolution of this technique to a few hundred femtoseconds.

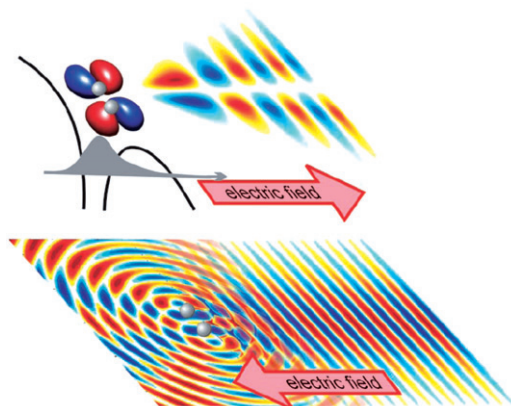


Figure 8. (Top) Tunnelling creates a filtered projection of the molecular orbital. Approximately half of the electron wave packet escapes directly to the detector. (Bottom) Remaining portion is driven back to the parent ion. Here, the central portion of the recolliding wave packet is shown diffracting from the molecule. The outer portions of the wave packet (not shown) weakly interact with the ion potential. The relative strength of each component depends on the filtered projection of the molecular orbital and therefore on molecular alignment. Reproduced with permission from M. Meckel et al. *Science* **2008**, 320, 1478. Copyright (2008) by AAAS. (The colour version of this figure is included in the online version of the journal.)

Such a limit can be overcome by the so-called laser induced electron diffraction (LIED) proposed in 1996 [64]. In this approach the molecule serves as its own photocathode, whereas the laser provides the accelerating field. This situation produces extremely high current densities and attosecond timing [65]. The first experimental observation of LIED is reported in [10] and the principle of the technique is depicted in Figure 8. Electrons escape from the molecule with a momentum distribution determined by the Highest Occupied Molecular Orbital filtered by the suppressed binding potential (top part of Figure 8). Almost half of them are created before the electric field reaches its maximum (absolute) value and then depart directly and irrevocably from its parent ion. Those freed, just after the field peaks, when the absolute value of the field is decreasing, do return to the ion where they can elastically scatter (diffract), inelastically scatter, or recombine to (interfere with) the orbital from which it was extracted thus producing High Order Harmonic Generation. Elastic and inelastic scattering occur at the molecular ion. Inelastic rescattering can cause multiple ionisation and subsequently lead to Coulomb explosion of small molecules. The molecular structure can then be inferred from the momentum vectors of the correlated ionic fragments. Elastic scattering is also sensitive to the molecular structure through the diffracting electron wave packet, making this imaging technique scaleable to more complex molecules.

For electron diffraction to be observable, the de Broglie wavelength of the electron needs to be on the order of the dimensions of the molecule. Electrons that are accelerated in the laser field and recollide with the parent molecule can easily reach more than 100 eV (corresponding to a momentum of 2.7 au) thus making possible the access to bond length of  $\approx 1 \text{ \AA}$  [1.9 atomic units (au)].

Recently this technique was demonstrated with electrons produced from aligned  $\text{O}_2$  and  $\text{N}_2$  [10], resolving their three-dimensional (3D) momentum distribution with the cold target recoil ion momentum spectroscopy (COLTRIMS) [66].

## 5. Attosecond XUV probes

### 5.1. Single attosecond pulses and train of attoseconds

The main route to generate attosecond radiation pulses is presently based on High-Harmonic Generation (HHG) in gases by means of ultra-intense femtosecond laser pulses [67,68]. The generation mechanism sets the spectral window of attosecond pulses in the XUV range.

Attosecond pulses by means of HHG have been obtained either as a periodic sequence of several pulses, separated by half the fundamental optical cycle in time from each other, named Attosecond Pulse Trains (APTs), or as a Single Attosecond Pulse (SAP) per each laser shot. APTs are obtained from multi-cycle fundamental pulses (see [69] for a recent and full experimental characterisation), whereas SAPs have been mostly generated by using few-cycle, Carrier-Envelope-Phase (CEP) stabilised laser pulses (see [70,71] for recent reviews).

When using APTs for attosecond control and metrology one has to make sure that the sub-cycle electron–light interaction is repeated over several oscillation cycles under precisely the same conditions, due to the temporal structure of the APT signal, shown in Figure 9.

Multi-cycle attosecond metrology basically relies on the idea that a well-known multi-cycle light wave triggers periodically repeated electron recollisions or, in a complementary vision, periodically repeated electron recollisions induce the emission of sub-fs photon pulse trains. One of the two correlated processes acts as a clock for the other, as first demonstrated in [65,72] for a diatomic molecule. To ensure that both the above processes unfold in the same way in each wave cycle, one would ideally use a light pulse with constant amplitude, namely having a flat-top intensity profile. Nevertheless, real multi-cycle drivers have bell-shaped envelopes. This implies often a non-negligible variation of the burst parameters across the APT. As a

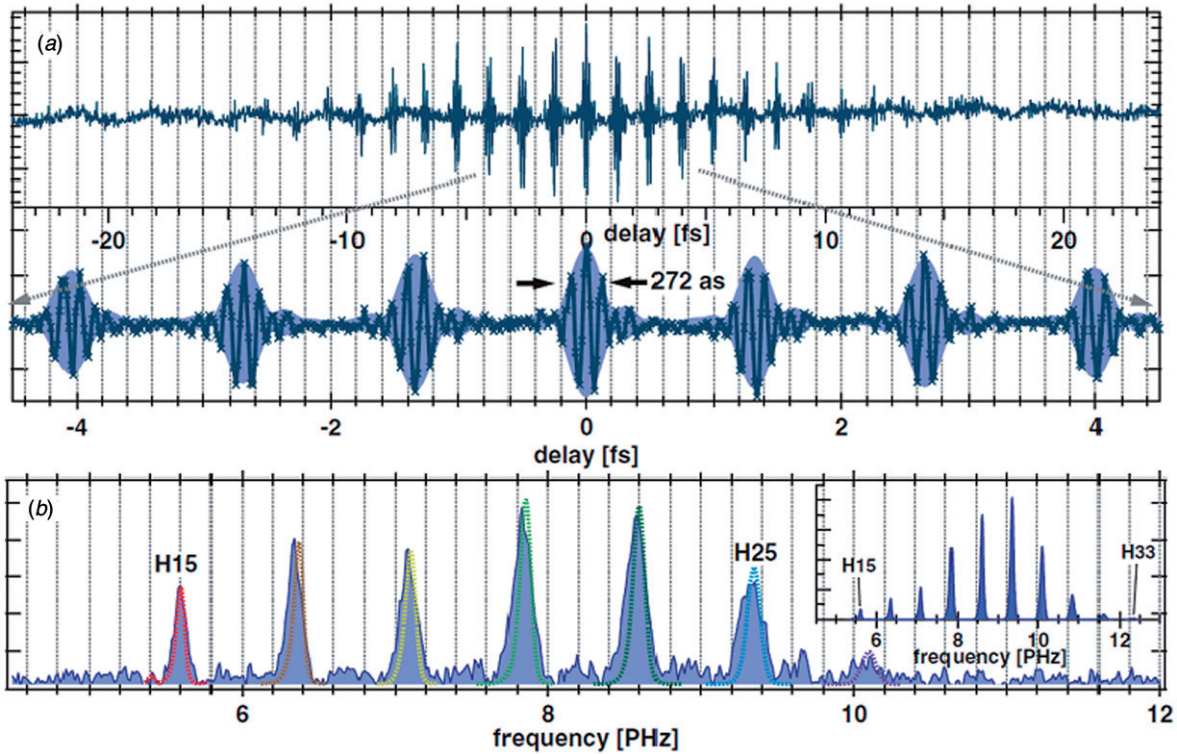


Figure 9. (a) Interference trace of the APT generated from Ar gas (top row) and a magnified view (bottom row). Cross markers correspond to the sampling points of scanned delay. (b) Magnitude of the Fourier transform of the APT interferometric trace, where the intensity has been arbitrarily normalised. Inset: observed intensity distribution in the XUV spectrograph. Reproduced with permission from Y. Nabekawa et al. *Phys. Rev. Lett.* **2009**, *102*, 213904. Copyright (2009) by the American Physical Society. (The colour version of this figure is included in the online version of the journal.)

consequence, even simple processes triggered by APTs can result in complicated temporal profiles, which makes high demand on the signal-to-noise ratio to be properly retrieved (see for instance [73,74] of the quoted list).

These problems can be overcome by using few-cycle attosecond technology, which is based on light waves consisting of well-distinguishable oscillation cycles with well-controlled temporal evolution. This permits triggering of a microscopic process within any selected wave cycle with sub-cycle temporal resolution, and leads to the generation of a single attosecond pulse per laser pulse.

When using few-cycle pulses to probe and drive the electron–light interaction CEP control cannot be discarded anymore. In fact, the response of electrons to such short light pulses is strongly dependent on the CEP value [75]. Control of the CEP of few-cycle laser sources, while commercially available nowadays for a few laser oscillators, it is still not trivial for amplified systems and implies a non-negligible effort even for the most advanced laser laboratories all over the world [76–78]. A first experimental demonstration of SAP generation is found in [78], using a 5 fs, CEP-stabilised

Titanium–Sapphire laser source. By filtering the highest-order harmonic emission with a XUV band-pass filter, and selecting a CEP equal to zero, the authors could generate a SAP, with an estimated duration of  $\approx 250$  as, spectrally centred around 90 eV (see Figure 10). The spectral counterpart of a SAP temporal structure is reported in Figure 10(a) where, for a cosine wave, a smooth spectrum appears in the harmonic cut-off region, indicating the emission of a single pulse with a sub-fs potential duration. This single emission event has a spectrum corresponding to the highest-order harmonic region. In Figure 10(b), for a sine-like wave-form there exist two peaks of the electric field with equal amplitude. As a consequence, a modulation appears in the spectrum as a result of the interference between the two coherent radiation bursts emitted half a cycle apart.

A disadvantage of the above technique is represented by the constraint to filter out only the highest-order harmonic region of the spectrum. This is dictated by the need to select those harmonics which are generated by no more than one or two electron recollisions in order to end up with a SAP. As a consequence SAPs result, in this case, to be spectrally

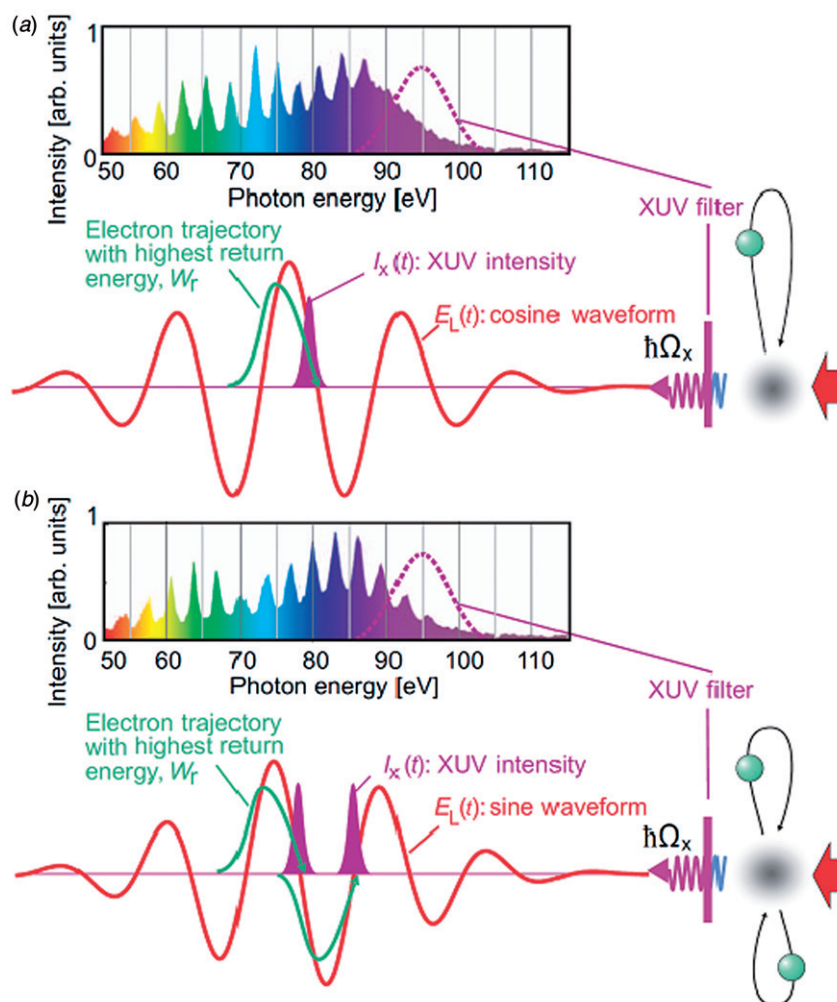


Figure 10. Measured HHG spectra with a few-cycle NIR pulse (5 fs, 750 nm) with (a) cosine-shaped and (b) sine-shaped waveforms [78] corresponding to CEP=0 and CEP= $\pi/2$ , respectively. Reproduced with permission from F. Krausz and M. Ivanov, *Rev. Mod. Phys.* **2009**, *81*, 163–234. Copyright (2009) by the American Physical Society. (The colour version of this figure is included in the online version of the journal.)

located in the 80–100 eV region, which is quite deep XUV and more suitable to study inner core electron rather than valence electron dynamics. Moreover, the number of XUV photons constituting the SAP is lower than it could be if one were able to generate SAPs from the plateau harmonics that typically fall in the 25–45 eV region of the spectrum.

For few-cycle, CEP-stabilised laser sources the polarisation gating method has been successfully implemented to give SAPs in the 250–300 as range, spectrally centred around 30–35 eV when using Ar as a nonlinear medium [79]. These SAPs have been fully characterised [80] by using a cross-correlation experimental technique which has a strong analogy with the streak-camera approach, but used to characterise pulses in the  $\sim 100$  as duration range. The basic idea of the cross-correlation measurements is the following: the SAP under investigation ionises a gas, by single

photon absorption, thus producing an attosecond electron pulse which, in the absence of any gas resonance, is a replica of the optical pulse. This occurs in the presence of a streaking IR pulse, whose electric field behaves as an ultrafast phase modulator on the generated electron current. The evolution of the photo-ionisation spectra as a function of the delay,  $\tau_d$ , between attosecond and IR pulses, allows one to retrieve the temporal intensity profile and phase of the XUV pulse and the electric field of the IR pulse. This technique has been called frequency-resolved optical gating for complete reconstruction of attosecond bursts (FROG CRAB) [81], just as it is conceptually and numerically analogous to characterise an optical pulse with the FROG technique in the femtosecond time scale. In Figure 11(a) photoelectron energy spectra as a function of  $\tau_d$  are reported as obtained in [80]. In that case Ar was used as a nonlinear medium

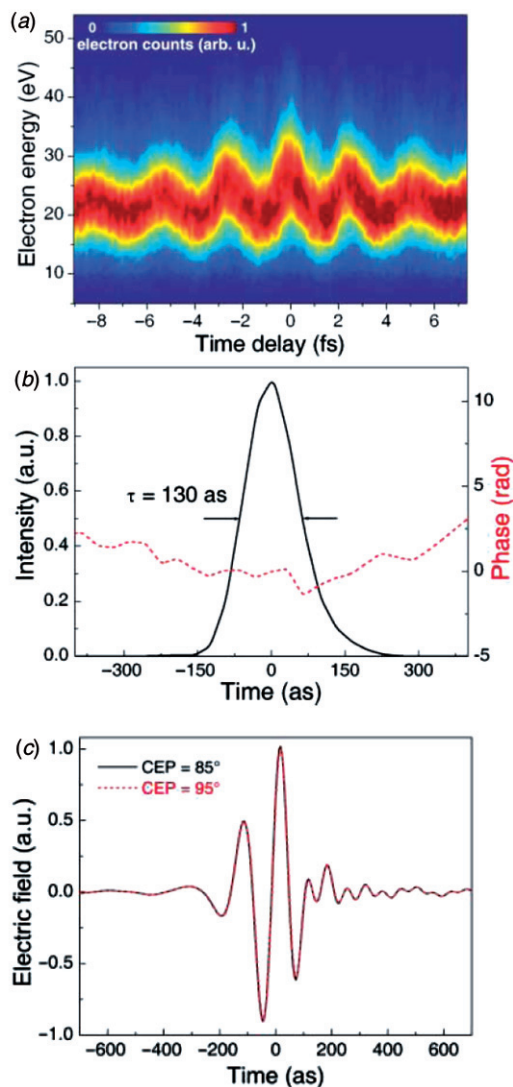


Figure 11. (a) Complete experimental CRAB trace measured as a function of the temporal delay between the attosecond and IR pulses. (b) Retrieval of temporal intensity profile and phase of SAPs obtained from the CRAB trace shown in (a). (c) Retrieved electric field of the SAP shown in (b) for two different values of the CEP of the driving field. Reproduced with permission from G. Sansone et al. *Science* **2006**, 314, 443. Copyright (2006) by AAAS. (The colour version of this figure is included in the online version of the journal.)

whereas the driving field was delivered by a 5 fs CEP-stabilised Titanium–Sapphire system. The electron energy, modulated in time with the IR pulse period, is centred at approximately 20 eV which implies a XUV spectral centre at  $\approx 35$  eV, given by adding the Ar ionisation potential to 20 eV. Figure 11(b) shows the result of the FROG CRAB retrieval applied to the measurement displayed in (a). After removal of the harmonic intrinsic positive chirp [82] by means of a 100 nm thick aluminium foil, which provides the necessary negative group delay dispersion to

compensate the initial XUV positive chirp, the SAP duration is measured to be 130 as (FWHM of the intensity). This duration implies a XUV electric field structure as reported in Figure 11(c) for two different CEP values, which shows a good stability of the generated SAP against the CEP fluctuations. Due to the longer carrier wavelength of this SAP as compared to that obtained at  $\approx 95$  eV, the electric field envelope just contains about 1.2 cycles, thus constituting the first few-cycle XUV-pulse to date.

Very recently the 100 as barrier has been broken. Using waveform-controlled sub-1.5-cycle NIR laser pulses and chirped XUV multi-layers for spectral filtering and dispersion control [83–85], SAPs as short as  $\approx 80$  as at  $\sim 85$  eV photon energy have been demonstrated [86]. The photon flux of these SAPs has been estimated in the range of  $\sim 10^{11}$  photons  $s^{-1}$ , allowing for time-resolved measurements of electron processes with a resolution approaching the atomic unit of time ( $\sim 24$  as).

Attosecond pulses have been so far demonstrated by means of high-order harmonic generation in gases, although such technique manifests a number of drawbacks that limit energy, duration, and the shortest possible wavelength centre of gravity of the generated pulses. These limitations arise from the fact that, using fundamental pulse intensities higher than the gas target saturation intensity, about all the atoms of the gas medium are ionised: this prevents efficient high-order harmonic generation from taking place since the time when the saturation intensity is reached. Moreover, when using CEP-stabilised few-cycle driving pulses, typically exploited for single attosecond pulse generation limitation, another severe constraint comes into play consisting of the relatively low driving pulse energy available so far, which limits the attosecond pulse energy to the sub-nJ energy range [79,86]. Numerous applications, based on nonlinear medium response in the XUV, such as nonlinear spectroscopy for instance, which typically require high spectral brightness, fall out of reach just considering high-order harmonic generation in gases. Quasi-phase-matching techniques have been implemented to increase the harmonic yield, based on generation in filled in capillaries [87] or in long media with mixed gaseous species at low pressure [88], but they have not been demonstrated for isolated attosecond pulses and, additionally, they are often effective for specific spectral windows, which can limit the bandwidth of the generated pulses and produce longer attosecond pulses.

High-order harmonic generation in laser-produced plasmas from solid targets can be a way to overcome the above limitations: intense laser pulses focused on solid surfaces lead to the formation of a hot plasma

that can act as an efficient nonlinear medium for high harmonic generation. Two different physical mechanisms have been invoked to explain high harmonic generation in this case, depending on the driving field peak intensity: coherent wake emission [89] and oscillation of the plasma surface at relativistic velocities [90]. However, since harmonic emission occurs in the laser-induced plasma, saturation of the medium ionisation is no longer a limitation, but a necessary prerequisite for the process to take place.

In the relativistic regime, in particular, where the generation of intense attosecond pulses in the deep XUV spectral domain is expected, harmonics from a solid target are emitted by a surface basically made of electrons freed by the leading edge of an extremely intense laser pulse, which can oscillate around an immovable ion background. Under such a condition, the interplay between the Lorentz force,  $F_{\text{Lorentz}} \propto \mathbf{v} \times \mathbf{B} \propto I_L \lambda_L^2 \sin(2\omega_L t)$ ,  $\lambda_L$  and  $\omega_L$  being the laser pulse carrier wavelength and frequency, respectively, which tends to move the electrons parallel to the laser polarisation direction, and the restoring force due to the electrostatic field induced by charge separation, leads to an oscillatory motion of the electron surface which determines harmonic emission. The expected harmonic conversion efficiency reaches a few percent in the  $\sim 10$  nm spectral region, which is a much higher value compared to that obtain in gases typically limited to  $10^{-4}$ – $10^{-5}$  in the plateau and  $10^{-7}$ – $10^{-8}$  in the cut-off region.

Recent works [91,92], however, have pointed out that a physical mechanism, other than that invoked in the oscillating mirror model, could be responsible for harmonic generation from solids in the relativistic regime. This theory has been named the relativistic  $\gamma$ -spikes model as it has been demonstrated that for most of the time of interaction between plasma and laser pulse, the relativistic  $\gamma$  parameter of the plasma mirror is close to one, except for a very short time window when the electrons move perpendicularly to the plasma surface and, in correspondence,  $\gamma$  presents a sharp spike, reaching its highest possible value  $\gamma_{\text{max}} = (1 + a_L^2)^{1/2}$ ,  $a_L$  being the laser pulse amplitude. This theory predicts that harmonic generation and attosecond bunching of the reflected radiation take place just at the  $\gamma$ -spike time. Interestingly, the oscillating mirror model and the  $\gamma$ -spike theory predict a different  $\gamma_{\text{max}}$ -scaling power law for the maximum frequency,  $\omega_{\text{max}}$ , of the emitted harmonic spectra:

$$\omega_{\text{max}} \propto \begin{cases} 4\gamma_{\text{max}}^2 \omega_L & \text{oscillating mirror,} \\ \omega_L \alpha^{1/2} \gamma_{\text{max}}^3 & \gamma\text{-spikes,} \end{cases} \quad (2)$$

$\alpha$  being a numerical factor of the order of unity [91]. An experimental test concerning harmonic generation

from solids in the relativistic regime has been carried out at the Rutherford Appleton Laboratories using the Vulcan Petawatt laser which delivers up to 600 J, 500 fs pulses for a highest achievable intensity of  $10^{21}$  W cm $^{-2}$  [93]. Harmonics up to 1.2 nm corresponding to the 850th order of the fundamental at 1054 nm were observed with harmonic pulse energies in the 0.07–0.7 mJ range at 4 nm and 0.2–20 mJ range at 17 nm. One year later the same group reported [94] the generation of the 3200th order, corresponding to 3.8 keV of the fundamental frequency from a CH target and studied the dependence of the harmonic spectrum cut-off on  $\gamma_{\text{max}}$ , finding out that experiments confirm the validity of the  $\gamma$ -spike rather than the oscillating mirror theory in the investigated regime of the  $\gamma$  parameter.

It is worth mentioning here that, in order to achieve the highest possible harmonic conversion efficiency it turns out that the plasma formation needs to be nearly completely suppressed until a few picoseconds before the main laser pulse. At intensities of the order of  $\sim 10^{20}$  W cm $^{-2}$  or even higher this condition implies a pulse contrast, peak over background level, of  $10^{10}$ – $10^{11}$  which, even though not a trivial task, has been recently obtained by using the plasma mirror technique.

## 5.2. Electronic motion in atoms

Electron excitations in atoms and molecules and consequent multi-electron processes are extremely fast, their dynamics typically ranging from tens of attoseconds to tens of femtoseconds. Direct time-domain access promises to shed light and give a deeper insight into these processes, especially core excitations, and to possibly suggest ways to control and affect them. As a possible near-future application, for instance, the research to develop and realise efficient and compact XUV and X-ray laser sources may strongly benefit from the investigation of the above processes with attosecond resolution. There are nowadays a considerable number of interesting applications of attosecond pulses to the study of the electronic motion in atoms such as, for example, triggering core-level excitation with consequent intra-atomic and molecular processes, including shake-up of one or more electrons and a number of possible decay phenomena, such as Auger, Coster–Kronig, or cascaded. Updated and exhaustive reviews on these studies are present in the literature [70,71]. Here we just report two recent examples of experiment which resolves the electronic motion in atoms based on the use of SAPs, the former, and of APTs, the latter. In the former experiment [16] the authors investigated the electronic motion in neon atoms on the attosecond

time-scale giving insight into the nonadiabatic tunnelling ionisation process.

The study performed by Uiberacker et al. is a good example of application of the attosecond tunnelling spectroscopy (ATS), where electrons shaken up to the valence band are released from negative-energy (bound) states by tunnel ionisation. ATS is based on counting ions of different charge states: as a first step a core electron is ejected by a sub-fs XUV pulse. A couple of very basic physical questions then arise: (i) how does the shake-up occur? (ii) is it instantaneous (as currently believed) or possibly delayed?

Theory [95,96] (see also [97] for a review of strong-field ionisation) predicts that both in the conventional tunnelling regime, where the ponderomotive potential,  $U_p$ , of the driving field can provide an energy much larger than that required to overcome the atomic potential barrier,  $W_b$ , and in the intermediate regime where  $W_b \approx I_p$ , ionisation and consequent release of electrons with binding energies of  $W_b \geq 10$  eV, by intense multi-cycle NIR and IR pulses, occurs via nonadiabatic tunnelling. In this process ionisation is substantially confined within small fractions of the half oscillation cycles near the wave crest of the field. A proof-of-principle ATS experiment [16] corroborated this prediction (see Figure 12).

A 250 as 95 eV pump pulse ionises a valence electron from a neon atom. The excess photon energy triggers shake-up, promoting an electron to an excited state in the valence band. A time-delayed 5 fs 750 nm waveform-controlled pulse probes the transient population of the shake-up states by field ionisation, resulting in doubly charged neon ions,  $\text{Ne}^{2+}$ . The steplike increase in  $\text{Ne}^{2+}$  yield with steps approximately separated by half the laser period provides evidence for optical field ionisation responsible for the depletion of excited valence states, in agreement with the theory developed in [95]. Shake-up and tunnelling occur within even less than  $\approx 400$  as, as the inset shows with good reproducibility from different measurements. With recently improved sources such as sub-1–5-cycle NIR waveforms [98] and sub-100 as XUV pulses [86], details of shake-up and nonadiabatic tunnelling dynamics are expected to be further clarified.

In the latter example, reported here below, the authors realise a quantum stroboscope based on an APT used to release atomic electrons in the presence of a strong IR laser field linearly polarised [99]. This is a very basic application of APTs to directly imaging coherent electron rescattering that takes place when the IR field is sufficiently intense to reverse the initial

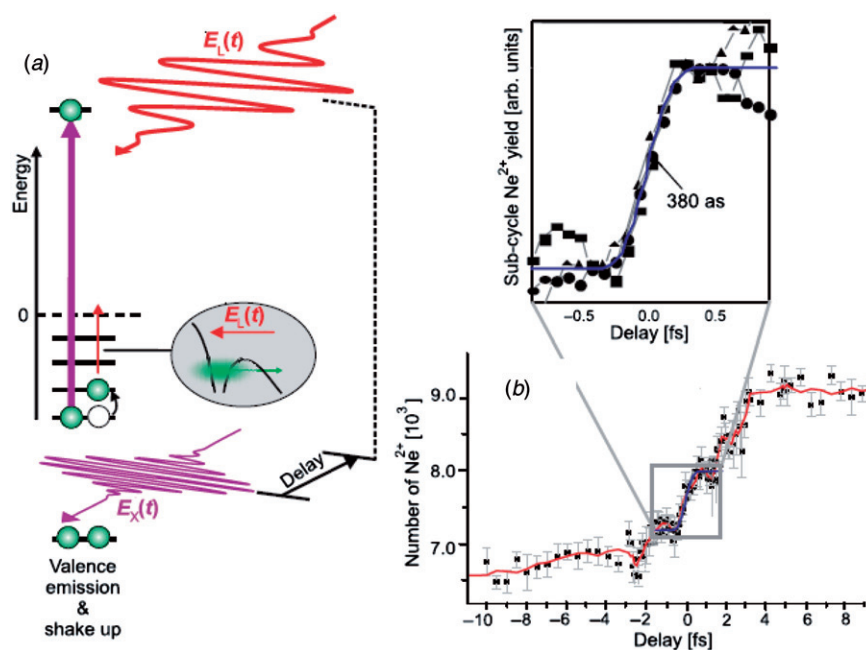


Figure 12. Attosecond real-time observation of light-field induced nonadiabatic electron tunnelling. (a) Principle of the measurement. (b)  $\text{Ne}^{2+}$  ion yield versus time delay between the 250 as XUV pump pulse and the 5 fs NIR probe pulse. The inset zooms into the central sub-cycle ionisation step, plotting data (dots, squares, triangles) obtained from different measurements. Reproduced with permission from M. Uiberacker et al. *Nature* **2007**, 446, 637. Copyright (2007) by Nature Publishing Group. (The colour version of this figure is included in the online version of the journal.)

direction of the electron motion, causing it to rescatter from its parent ion.

When neglecting the influence of the atomic potential [100], the momentum of an electron created at time  $t_0$ , viewed as a function of time,  $t$ , reads as [99]:

$$\mathbf{p}(t, t_0) = \frac{eE_0}{\omega} [\cos(\omega t_0)\hat{y} - \cos(\omega t)\hat{y} + \gamma\hat{u}], \quad (3)$$

where  $e$  is the electron charge,  $E_0$  and  $\omega$  are the IR field amplitude and carrier frequency, respectively,  $\gamma = [(E_{\text{xuv}} - I_p)/2U_p]^{1/2}$ ,  $E_{\text{xuv}}$  and  $I_p$  being the XUV photon energy and atomic ionisation potential, respectively,  $U_p = e^2 E_0^2 / 4m\omega^2$  the quiver energy of the released electron of mass  $m$  in the IR pulse,  $\hat{y}$  and  $\hat{u}$  are the IR field polarisation and initial direction of the outgoing electron, respectively. Thus, it is seen that Equation (3), which describes the wiggling motion of the electron into the IR field, is made up of two contributions to the electron momentum, the former due to the IR field which depends on  $t$  and  $t_0$ , the latter representing the initial momentum of the outgoing electron released by photo-absorption from APT. In the end, the authors map the final (drift)

momentum:

$$\mathbf{p}_f(t_0) = \frac{eE_0}{\omega} [\cos(\omega t_0)\hat{y} + \gamma\hat{u}], \quad (4)$$

which is obtained from Equation (3) by just switching off the IR field at later times. In order to observe coherent scattering, the electron, once released, must pass the ion core at least once. It is then seen from Equation (4) that the final momentum can be zero or opposite to the initial momentum, for certain delays, if  $\hat{y} \parallel \hat{u}$  and  $\gamma \leq 1$ .

The principle of the quantum stroboscope is illustrated in Figure 13 together with some of the experimental results. An APT, constituted by a sequence of identical attosecond pulses, is used to release electrons in the presence of an IR laser field exactly once per laser cycle. The generated electron wave packets (EWPs) disperse as they fly towards the detector where their momentum distribution is recorded. Consecutive EWPs will therefore overlap and interfere. Since the impulse imparted to the electron by the IR field depends on the ionisation time [101–103], each phase of the oscillating laser field

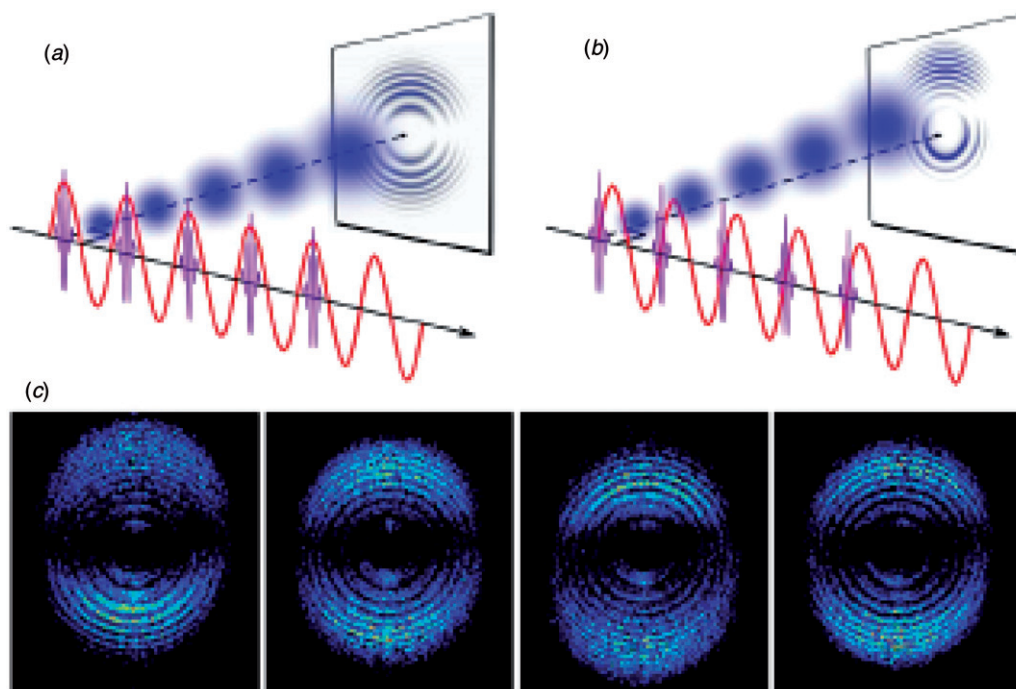


Figure 13. (a)–(b) Principle of the quantum stroboscope. An APT ionises the target atom once per cycle of an IR laser field. When the EWPs are created at the maxima of the IR electric field (a), the net transfer of the momentum is zero and resulting momentum distribution is symmetrical relative to the plane orthogonal to the laser polarisation. When the EWPs instead are created at the zero-crossings of the IR electric field (b) the momentum distribution is shifted by the field along the laser polarisation direction. (c) Experimental results obtained in argon at four different delay values: from left to right the images correspond to the XUV-IR delays  $t_0 = 0, \pi/2\omega, \pi/\omega, 3\pi/2\omega$  for an IR intensity of  $5 \times 10^{12} \text{ W cm}^{-2}$ . Reproduced with permission from J. Mauritsson et al. *Phys. Rev. Lett.* **2008**, *100*, 073003. Copyright (2008) by the American Physical Society. (The colour version of this figure is included in the online version of the journal.)

gives rise to a unique final momentum distribution. When the attosecond pulse periodicity matches the IR optical cycle, the created EWPs are affected identically by the IR field, with the result that the dynamics of individual events can be studied stroboscopically. In contrast, if ionisation occurs over the whole IR cycle, or even at as few as two times during the cycle, the resulting momentum distribution will be smeared out and show interference fringes that depend on the different ionisation times. The quantum stroboscope shares two important features with a conventional stroboscope and essentially exploits in its essence the temporal structure of APTs rather than that of SAP signals. First, it is possible to freeze the periodically varying momentum distribution at a single phase of the IR field, and capture the full time-dependent distribution by varying the XUV-IR delay. Second, by repeating the process periodically, the measured signal is stronger than what one would measure with a single pulse. In the quantum stroboscope, the signal is further enhanced due to the coherence of the process, in that a train of  $N$  pulses yields fringes that are  $N^2$  times brighter than the signal originating from a single pulse of the sequence, though the essential requirement is to have  $N$  identical pulses, which is not always the case in practice. The quantum stroboscope technique may in principle provide a complementary approach to the use of SAPs, in particular, suitable for experiments where a high signal-to-noise ratio is required.

### 5.3. Electronic motion in molecules

The extension of APTs and SAPs to ultrafast imaging of small molecules (as treated in Section 5.2 of this review) is obvious but here we concentrate on possible applications to larger systems such as bio-molecules. In particular, we will dedicate a few notes on the charge migration process in bio-molecules which interconnects two fields that have been thought to be far apart from each other until now, i.e. attosecond science and dynamics in bio-systems.

Charge migration in bio-molecules is a particularly exciting process, as recent studies [104–109] suggested that its dynamics should range from a few femtoseconds to tens of attoseconds, thus unexpectedly linking the physics at the sub-fs time-scale, which is typically concerned with simple systems such as atoms or simple molecules, to processes that govern the evolution of complex systems such as proteins, nucleic acids, and their constituents.

Charge transfer is a crucial process in nature, playing a fundamental role in several chemical, biological, and physical processes. Photosynthesis is an obvious example of a chemical change triggered by an

ultra-fast electronic event but there are many other such reactions which involve proteins. As demonstrated in [104,106,109] purely electronic effects are essential to drive charge transfer, preceding any sort of nuclear rearrangement in the bio-molecule. In such a case the charge transfer process is referred to as charge migration. This ultrafast charge dynamics is typically triggered by sudden removal of one electron from a neutral molecule which gives rise to a non-stationary electronic state whose evolution is strongly affected by electron correlations. Following localised and prompt ionisation charge migration has been investigated in a number of electronic systems [105,107] by calculating the spatio-temporal evolution of the hole density generated by the initial excitation. The hole density is defined as the difference between the electron density of the neutral and that of the cation:

$$\begin{aligned} Q(\mathbf{r}, t) &= \langle \Psi_0 | \hat{\rho}(\mathbf{r}, t) | \Psi_0 \rangle - \langle \Phi_i | \hat{\rho}(\mathbf{r}, t) | \Phi_i \rangle \\ &= \rho_0(\mathbf{r}) - \rho_i(\mathbf{r}, t), \end{aligned} \quad (5)$$

where  $|\Psi_0\rangle$  is the ground state of the neutral,  $|\Phi_i\rangle$  the non-stationary state generated by the sudden excitation,  $\hat{\rho}$  is the density matrix operator,  $\rho_0(\mathbf{r})$  and  $\rho_i(\mathbf{r}, t)$  are the electron densities in the ground and non-stationary state, respectively. Equation (5) can be recast as:

$$Q(\mathbf{r}, t) = \rho_0(\mathbf{r}) - \rho_i(\mathbf{r}, 0) + \Delta\rho(\mathbf{r}, t), \quad (6)$$

where the first two terms are time-independent and describe the density of the initially created hole  $Q(\mathbf{r}, 0)$ , whereas the last term, time-dependent, describes charge migration driven by electron correlations. A number of methods have been developed to follow the temporal evolution of  $\Delta\rho(\mathbf{r}, t)$ , from time-dependent perturbation theory [105] to *ab initio* calculations, where a large number of eigenstates and eigenenergies of the ion created by the removal of an electron are evaluated [108]. As an example of the obtained results Figure 14 shows the calculated hole occupation as a function of time for an atom (Kr), a small molecule ( $\text{CO}_2$ ), and for a complex molecule (*N*-methyl acetamide  $\text{CH}_3\text{-CO-NH-CH}_3$ ). Despite the great difference in the nature of the investigated systems the hole occupation monotonously decreases, quickly in time, up to 50 as in all cases. After that time a different charge migration mechanism sets in with characteristics specific for each system. However, the computed evolution is extremely fast in all cases, exhibiting its features on the few-hundred-attosecond time-scale: pump-probe measurements with attosecond resolution have been proposed to investigate such ultrafast relaxation dynamics. Another very illuminating study concerns charge migration in complex real bio-molecules such as the Tryptophan terminated

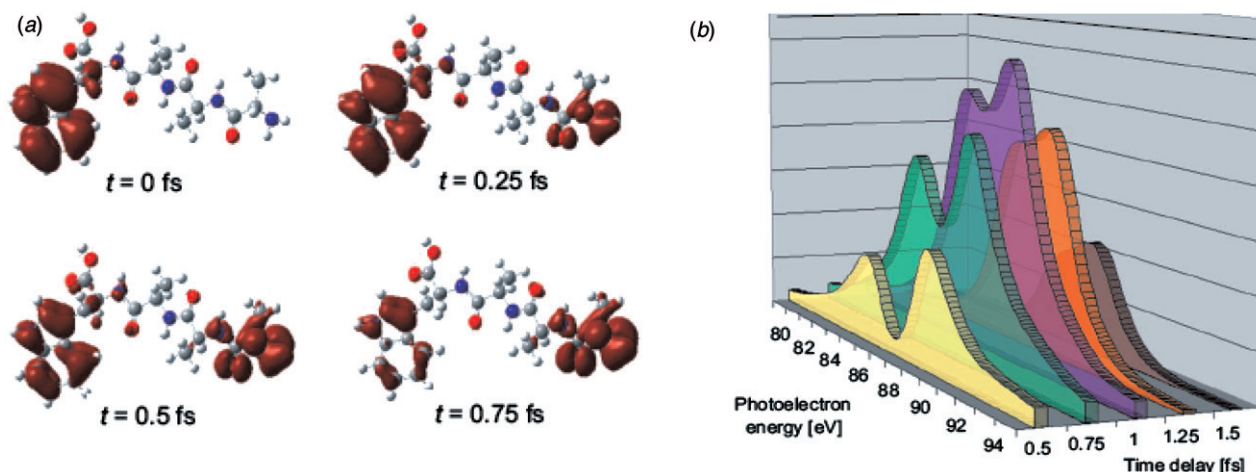


Figure 14. Computed ultrafast positive charge migration in a tryptophan-terminated tetrapeptide [109]. (a) The hole density, represented in red, indicates that the charge migrates across the whole peptide from the aromatic amino acid to the N end on the right within less than one femtosecond. The excitation dynamics of the electron wavepacket follows an attosecond time-scale. (b) Series of photoelectron energy spectra calculated for a 250 as 95 eV probe pulse, time-delayed with respect to the sudden ionisation of the biomolecule. Reproduced with permission from F. Remacle and R.D. Levine, *Z. Phys. Chem.* **2007**, *221*, 647. Copyright (2007) by Oldenbourg Wissenschaftsverlag. (The colour version of this figure is included in the online version of the journal.)

tetrapeptide Trp–Leu–Leu–Leu, Trp and Leu denoting the amino acids Tryptophan and Leucine, respectively [109]. In this case a hole generated by sudden ionisation of the highest-occupied molecular orbital (HOMO) of the tetrapeptide, localised on the Trp end which is likely ionised being an aromatic amino acid, is expected to migrate to the other end of the biomolecule in about 750 as, as reported in Figure 14(a).

Interestingly it is found that the photoelectron energy spectra, calculated for a 250 as 95 eV ionising probe pulse in the present case, are strongly time-dependent. This is shown in Figure 14(b) and is due to the manner in which contributions of different orbitals of the cation to the photoelectron spectrum varies with time. As a consequence, the kinetic energy distribution of the photo-electron will swing with time, following the temporal variation in the weights of the different orbitals of the cation in the non-stationary state that is pumped by sudden ionisation [110]. Thus, by monitoring photo-electron energy spectra with a pump–probe scheme, for example, where the probe could be a well characterised few-cycle CEP-stabilised IR pulse, one could charge migration dynamics with attosecond resolution. From the purely experimental point of view, these theories have been indirectly corroborated by the seminal experiments reported in [111,112] where charge transfer in peptide cations has been investigated, demonstrating that the peptide ions dissociate at a site far away from the initial ionisation site, though the time-scale of the process has not been experimentally determined yet.

Recently a very exciting result has been obtained concerning the electron delocalisation time in genomic DNA periodic backbones [113]. Based on a powerful but indirect technique, the so-called core-hole clock method [114], this time is estimated to be  $\sim 740$  as. The experiment reported in [113] makes use of Resonant Auger Spectroscopy (RAS) which makes possible to monitor delocalisation of an initially-localised core-excited state around the absorption atom. An X-ray source with energies between 2150 and 2160 eV (at the High Energy Accelerator Research Organisation – Tsukuba, Japan), excited the P 1s core electron of the DNA sample to an empty orbital of the DNA backbone (see Figure 15(a)). Two competing decay channels follow such excitation, associated with core-hole decay and core-excited resonant electron delocalisation, respectively, giving rise to two distinct types of RAS spectra: the former decay path is characterised by a main Auger emission peak at about 1857 eV whereas the latter path exhibits the corresponding Auger emission peak at about 1852 eV. In the core-hole decay (see Figure 15(b)) the excited electron remains sufficiently long to be localised in the proximity of the core-hole site and the final state is represented by two holes with one electron ( $2h1e$ ), process known as ‘spectator Auger decay’. When the excited electron delocalises to the conduction band prior to the core-hole decay (see Figure 15(c)) the decay process results in a final state of two holes ( $2h$ ), known as ‘normal Auger decay’.

For the case in which the time scale of delocalisation is comparable to the core-hole decay, both the

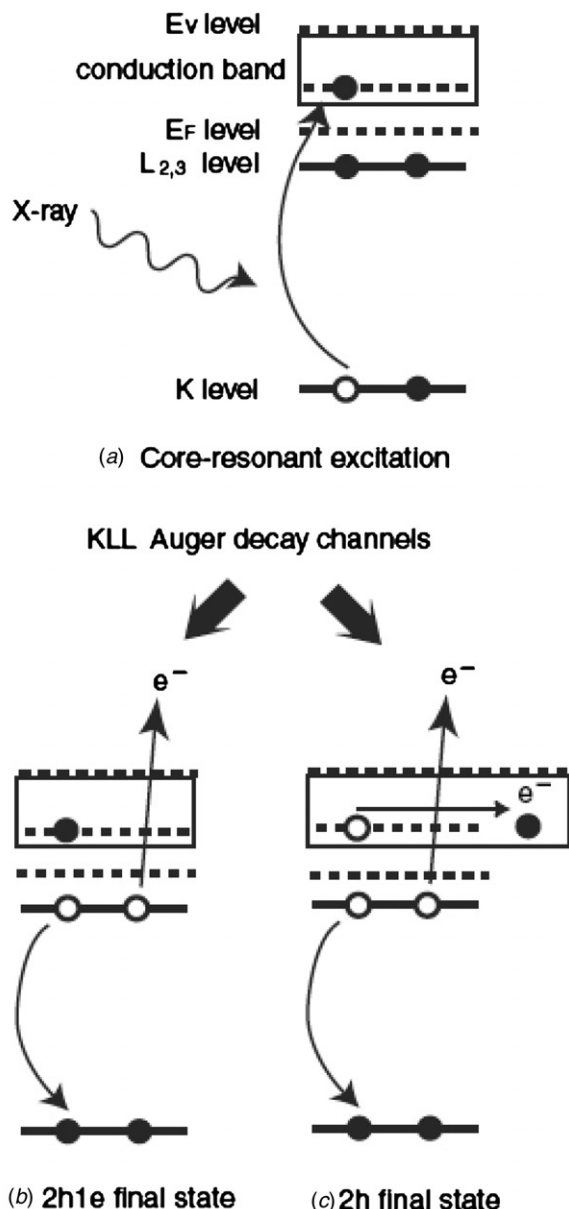


Figure 15. (X-ray Absorption Spectroscopy)–(Resonant Auger Spectroscopy) scheme used to retrieve the electron delocalisation time in genomic DNA periodic bones [113]. (a) Phosphorus  $1s$  core electron excitation into an unoccupied state of the conduction band. (b) Spectator Auger final state ( $2h1e$ ) caused by localisation of the excited electron to the core-hole site. (c) Normal Auger final state ( $2h$ ) caused by delocalisation of the excited electron to the conduction band coupling to the continuum.

spectator and the normal Auger are visible. By quantifying the intensity ratio of the two Auger emissions one can retrieve the electron-delocalisation time, based on the core-hole clock, in which the core hole acts as a fast internal clock, its lifetime ranging from femtoseconds down to attoseconds [115].

It is clear, then, that from experiments such as the one reported above, the consequences of which might be enormously important to many areas of science, a strong demand arises for a new generation of attosecond light sources, able to join sub-femtosecond pulse duration and wide tuneability in the X-ray domain. Such sources could allow the investigation of the above processes directly in the time domain with no need of complicated retrieval procedures, likely providing a much better temporal resolution. From this point of view recent advances performed in designing and setting up the latest generation of ultrashort XFELs look very promising as sub-fs durations of widely tuneable pulses are expected still carrying a remarkable number of photons [116,117].

#### 5.4. Electron dynamics in solids and surfaces

Over the last five years attosecond science has been applied to solid state and surface physics. Amongst these various applications we shall mention here two very interesting experiments concerning (i) the use of attosecond spectroscopy to observe the electronic charge transport in a tungsten crystal [17] and (ii) the proposed measurement of collective electron oscillations in nanostructures with attosecond temporal resolution and nanometre-scale spatial resolution in a surface nanoplasmon [118]. We also remind the readers the review paper [119] for recent advances in VUV photoelectron spectroscopy of ultrafast surface processes.

As for the first application to a crystal material [17], it follows the first observation of the laser-assisted photoelectric effect from a solid [120]. With reference to Figure 16(a), where the experimental layout is drawn, photoelectrons are liberated in a tungsten crystal by a 300 as 95 eV SAP in the presence of a 5 fs 750 nm waveform-controlled pulse. Both pulses,  $p$ -polarised, impinge at grazing incidence on the sample. Figures 16(b) and (c) represent the unperturbed XUV-induced photoelectron energy spectrum and the corresponding streaking spectrogram, respectively. Core-level electron emission from the  $4f$  level, around 55 eV, and valence-band electron from the Fermi edge, around 90 eV, are clearly visible. In particular, the energy spectrum is modulated with the NIR field period as a function of the delay between the two pulses (Figure 16(c)). Both the delocalised conduction-band electrons released from states near the Fermi edge and the localised core electrons originating from the  $4f$  state are found to have a sub-fs emission time. In Figure 16(d) the centre-of-mass energy shift of the recorded streaked spectra reveal

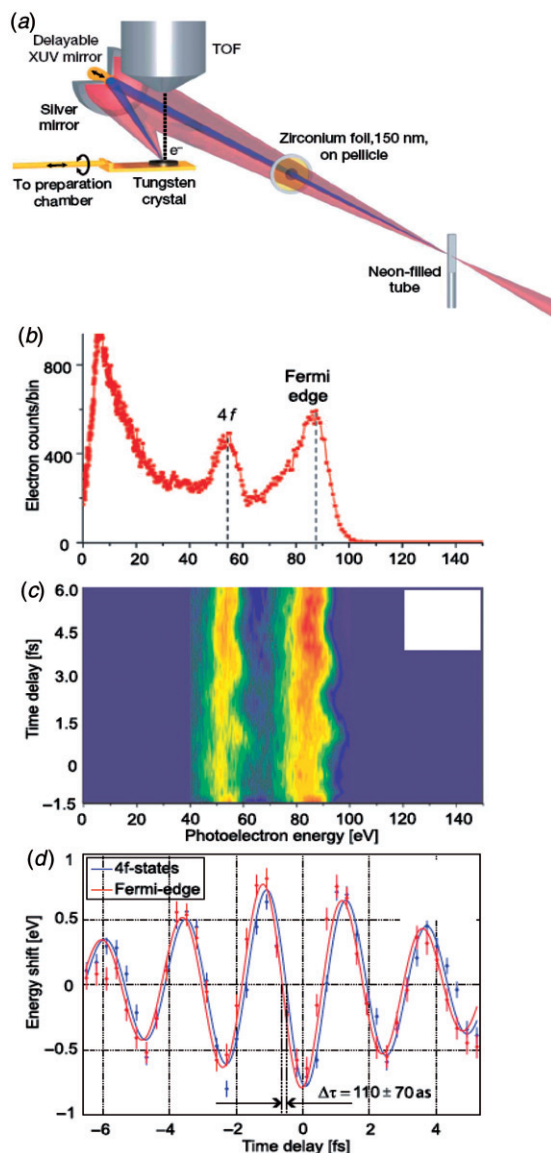


Figure 16. (a) Scheme of the experimental layout. (b)–(c) Unperturbed XUV-induced photoelectron spectrum and the corresponding streaking spectrogram recorded with the few-cycle NIR field, respectively. (d) The energy centre-of-mass of the recorded streaked spectra of the 4f electrons shifts of 110 as with respect to spectra of the Fermi-edge electrons. Reproduced with permission from A. Cavalieri et al. *Nature* **2007**, 449, 1029. Copyright (2007) by Nature Publishing Group. (The colour version of this figure is included in the online version of the journal.)

a  $\sim 110$  as delay in the emission of core electrons with respect to the emission of conduction band electrons.

The second application [118] proposes an attosecond nanoplasmonic field (ANPF) microscope by combining the temporal resolution of XUV SAPs and the spatial resolution of photoelectron emission spectroscopy (PEEM). A near-IR few-cycle light pulse with phase-stabilised electric field induces a

nanoplasmonic on a target which is a random planar composite made of silver nanometric. Being that the generated surface plasmon is confined to a nanostructure, a strong local field enhancement occurs with respect to the driving laser field. The ANPF is expected to directly measure the spatio-temporal dynamics of the enhanced local field (see Figure 17), by focusing onto the target a 200–400 as 90 eV SAP, synchronised with the near-IR pump pulse. The XUV SAP induces electron photoemission from the target with variable delay, the locally enhanced plasmonic field modulating the final energy of the photoelectrons. Thus, upon measuring the photoelectron energy spectra as a function of the time delay between the two pulses it is possible to retrieve the temporal evolution of the local electric field. Interestingly, this is an application of the streak camera concept, where the streaking field is given by the locally enhanced field. The temporal resolution of the proposed ANPF is limited so far, by the SAP duration, to about 100 as. Spatial information is obtained by imaging the excited nanoplasmonic system in a PEEM having energy resolution. The achievable spatial resolution is finally determined by the electron optics of the PEEM, being currently of the order of nanometres.

Hence, by using the proposed ANPF microscope, it will be possible to study collective electron excitations for the first time, thus going beyond the investigation of single- or few-active electron dynamics, which is the limit of attosecond science applied to the physics of atoms and simple molecules.

## 6. High-order harmonic generation as a probe for molecular structure

In the last 10 years the study of HHG from molecules has led to the realisation that the HHG spectrum encodes molecular structural and dynamical information with exceptional temporal and spatial resolution. There is currently a very active effort being expended to explore to what extent this information can be read-out with high fidelity.

### 6.1. Molecular alignment

The capability to fix the molecular frame axis in the laboratory has been vital in order to use HHG as a tool to probe the molecular orbital. Here we summarise the basic physical principles underlying the laser induced molecular alignment whose extensive treatment can be found in [121] (see also [122]). There are two alternative ways of using a strong laser field to align molecules with no permanent dipole moment. If the laser is turned on and off slowly as compared to the rotational

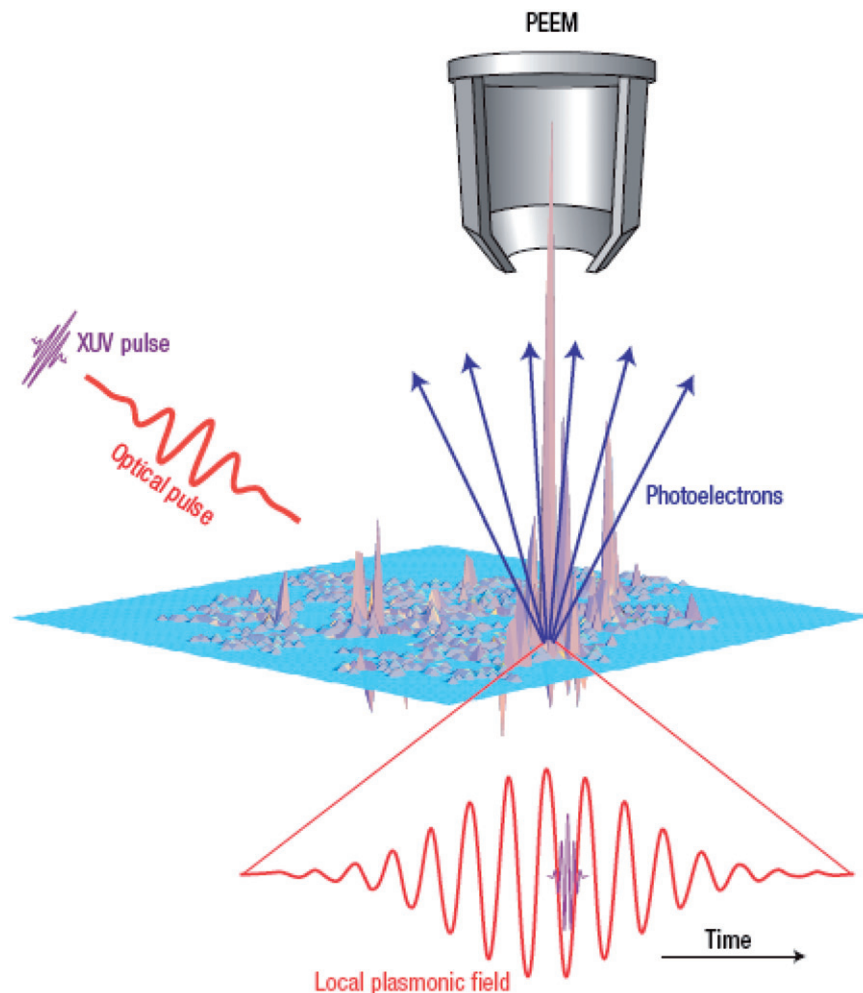


Figure 17. Principle of the Attosecond Nanoplasmonic Field (ANFP) microscope and related photo-processes. Instantaneous local fields, excited by the optical pulse, are shown as a three-dimensional plot. The local optical field at a maximum point ('hottest spot') is shown as a function of time by a red waveform, enhanced with respect to the excitation field. The XUV attosecond probe pulse causes the emission of photoelectrons represented by the blue arrows, which are accelerated by the local plasmonic potential. These electrons are detected by a PEEM with spatial and energy resolution. Reproduced with permission from M.I. Stockman et al. *Nat. Photon.* **2007**, *1*, 539. Copyright (2007) by Nature Publishing Group. (The colour version of this figure is included in the online version of the journal.)

period of the molecule, the alignment proceeds adiabatically. The interaction with the external electric field creates a so-called 'pendular' state which correlates adiabatically with the field-free rotational eigenstates [123] and, as the laser pulse fades away, the molecular ensemble returns smoothly to the isotropic angular distribution. This technique is termed 'adiabatic alignment'.

The other technique employs laser pulses much shorter than the rotational period of the molecule. In this case, the interaction leaves the molecule in a coherent superposition of rotational eigenstates. In order to have a significant degree of order in angular space, the different components of the wave packet

must keep a particular phase relation. A rotational wave packet freely evolving in time suffers a periodic dephasing (molecular axis orthogonal to the aligning electric field, so-called anti-aligned peak) and re-phasing (molecular axis preferentially aligned along the direction of the aligning electric field, so-called aligned peak) of its components, thus the aligned state only lasts for a short while, but it is periodically reconstructed at multiple revival times which persist for a long time after the interaction, until the collisions with other molecules break the quantum coherence. This technique is known as 'impulsive alignment' because the interaction with the short laser pulse can be viewed as a 'kick' imparted to the molecule.

Both methods have advantages and drawbacks which must be considered depending on the application of the aligned molecules. The adiabatic technique requires temporally smooth pulses of ns to  $\approx 100$  ps duration. Generally it provides a high degree of alignment during the laser pulse, and makes multi-axis alignment relatively easy to implement by the use of elliptically polarised fields, however, the presence of the aligning field can critically disturb the strong field processes which are the subject of investigation in most cases. The impulsive method has the advantage of generating field-free aligned molecules, and the process is not sensitive to the details of the pulse shape. Field-free alignment in 3D can be obtained by a method which utilises two orthogonally polarised time-separated laser pulses [124].

## 6.2. Molecular imaging of simple molecules ( $N_2$ and $CO_2$ )

With the molecules fixed in space we can use the HHG process to probe the molecular structure. HHG in the strong field limit can be seen as a three step process [125]: (i) ionisation; (ii) acceleration in the laser field; (iii) recombination back into the bound electronic state (recollision). The recollision of the electron is a brief event, taking much less than an optical period, and occurs at a well-synchronised moment with respect to the ionisation, and with an appreciable momentum (returning with kinetic energy in the 10–100 eV range for typical fields). As a consequence of these properties the recollision electron can be used as a probe in several ways. For instance, Corkum and colleagues first pointed out that the ionisation event forms correlated electron/nuclear wavepackets in a molecule; these can be used to determine vibrational or dissociation dynamics from measurements of the kinetic energy released when the molecules are collisionally ionised by the returning electron. In principle, the elastically scattered electron momentum distribution carries structural information through the interferences between the amplitudes arising from different scattering centres (electron diffraction), a process termed laser induced electron diffraction. Recently there have been advances both theoretically [64,126–129] and experimentally [10] towards realising this concept. It is, however, the emission of harmonics from a molecular target of aligned molecules that has been shown most successfully to carry structural information about the molecule with the potential for a very high temporal resolution [7,130–134]. This is possible because the HHG amplitude is dependent upon the dipole amplitude for the transition between the continuum state and the ground state. As the return electron energy is

in the range of 10–100 eV, the de Broglie wavelengths in the wave packet span the spatial scales of interest in the ground state wavefunction and so the dipole is sensitive to the electronic structure of the molecular ground state [7]. For a strong field linearly polarised along the direction  $\hat{e}$  the harmonic spectrum from a single emitter is proportional to the square of the Fourier transform of the dipole acceleration [135]

$$\begin{aligned} S_{\hat{e}}(\Omega) &\propto |\hat{e} \cdot \mathbf{a}(\Omega)|^2 = \left| \hat{e} \cdot \int \exp(i\Omega t) \ddot{\mathbf{d}}(t) dt \right|^2 \\ &= \Omega^4 \left| \int \exp(i\Omega t) \hat{e} \cdot \mathbf{d}(t) dt \right|^2 = \Omega^4 |d_{\hat{e}}(\Omega)|^2. \end{aligned} \quad (7)$$

This is the spectrum of harmonics polarised along the direction of the unit vector  $\hat{e}$ . In the following, we take  $\hat{e}$  parallel to the laser polarisation axis since the perpendicularly polarised harmonics are usually much weaker [131]. In Equation (7)  $d(\Omega)$  is the Fourier transform of the time-dependent dipole moment (length gauge), i.e.  $d_{\hat{e}}(t) = \langle \Psi(\mathbf{r}, t) | -e\mathbf{r} \cdot \hat{e} | \Psi(\mathbf{r}, t) \rangle$ , where  $\Psi(\mathbf{r}, t)$  is the time-dependent electron wave function evolving in the combined atomic/molecular and laser field potentials. The induced dipole is a measure of the charge displacement within the atom/molecule due to the electronic response to the applied field, thus  $\mathbf{r}$  has the same direction of the polarised laser beam inducing HHG. When the wave-function  $\Psi(\mathbf{r}, t)$  is written in terms of a superposition of bound and continuum parts (i.e.  $\Psi(\mathbf{r}, t) = \alpha\psi_0(\mathbf{r}, t) + \beta\psi_c(\mathbf{r}, t)$ ) and the wavefunction  $\psi_c(\mathbf{r}, t)$  is expanded as a sum of plane waves, the harmonic signal can be expressed as

$$S(\Omega) \propto \Omega^4 |a(\omega) \langle \psi_0 | -e\mathbf{r} \cdot \hat{e} | \exp[i\mathbf{k}(\omega) \cdot \mathbf{r}] \rangle|^2 \delta(\Omega - \omega - I_p). \quad (8)$$

In the above equation the ground state energy is  $E_0 = -I_p$  ( $I_p$  is the ionisation potential of the atom/molecule) and the function  $\mathbf{k}(\omega)$  and its inverse  $\omega(\mathbf{k})$  relate the plane wave momentum  $\mathbf{k}$  to its kinetic energy  $\omega$  as  $\omega(\mathbf{k}) = k^2/2$ . The  $\delta$ -function in Equation (8) is the expression of the energy conservation and indicates that the frequency of the emitted radiation is given by the sum between the kinetic energy  $\omega$  of the recolliding electron and the ionisation potential as expected from the strong field approximation theory [136].

Equation (8) reveals transparently how the dipole (which governs the radiation amplitude and phase) is directly related to the properties of the ground state wavefunction and the continuum. With the explicit and simple form for the continuum wavefunction assumed here, in principle, the ground state wavefunction can be retrieved from complete measurements of the

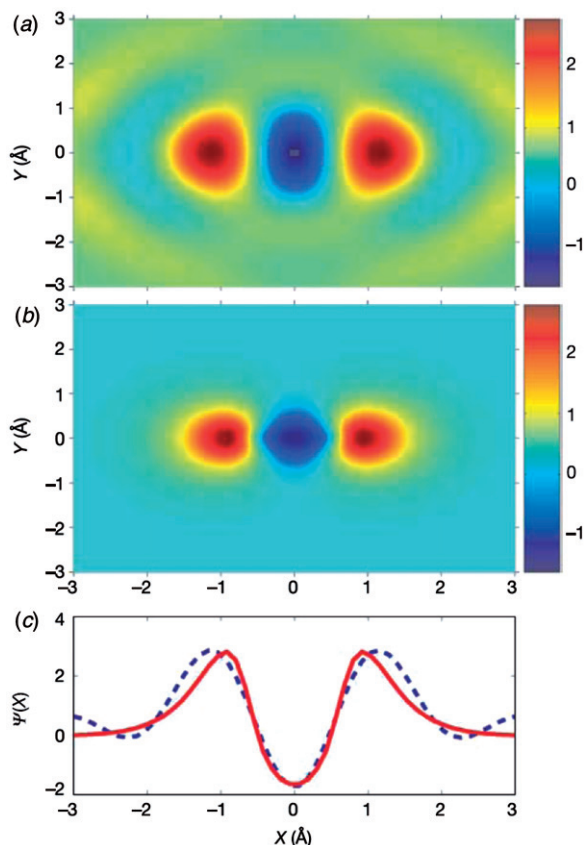


Figure 18. Molecular orbital wavefunction of  $N_2$ . (a) Reconstructed wavefunction of the HOMO of  $N_2$ . The reconstruction is from a tomographic inversion of the high harmonic spectra taken at 19 projection angles. Both positive and negative values are present, so this is a wavefunction, not the square of the wavefunction, up to an arbitrary phase. (b) The shape of the  $N_2$   $2p\sigma_g$  orbital from an *ab initio* calculation. The colour scales are the same for both images. (c) Cuts along the internuclear axis for the reconstructed (dashed) and *ab initio* (solid) wavefunctions. Reproduced with permission from J. Itatani et al. *Nature* **2004**, 432, 867. Copyright (2004) by Nature Publishing Group. (The colour version of this figure is included in the online version of the journal.)

harmonic phase and amplitude. This discussion is naturally extended to molecules as in our discussion no assumption has been made about the emitter. One way to do this is to perform the same experiment with a reference atom (sometimes called ‘companion atom’) whose ionisation potential is very similar to that of the molecule: in fact, the molecule and the companion atom have very similar response to strong laser fields. That means that the first, critical, step in the three-step high harmonic generation process is the same. Because the laser field dominates wave packet motion in the direction of the laser field, the second step, which determines the chirp of the re-colliding wave packets seen by the atom or molecule, will be the same.

Thus,  $a[k(\omega)]$  will be the same. This experiment has actually been done for the first time by Corkum’s group [7] where they used the harmonic spectrum from argon to determine  $a[k(\omega)]$  in order to be able to use Equation (8). The tunnel ionisation, due to its nonlinearity, is extremely selective and ionises only the highest electronic state, i.e. HOMO, which can be reconstructed (see Figure 18) by recording the harmonic spectra at a series of angles of the molecular alignment and then applying the orbital reconstruction method similar to medical tomography. Although the mathematical procedure applied in [7] can only be applied to reconstruct orbital shapes with symmetries such as  $\sigma_g$ ,  $\pi_g$  and  $\pi_u$ , the agreement between theory and experiment shown in Figure 18 is noticeable.

Numerical treatments of HHG have been carried out by solving the time-dependent Schrödinger equation for the simple molecules  $H_2^+$  and  $H_2$  [132,137,138]. It was found that as the angle  $\theta$  between laser polarisation and the internuclear axis was varied, for a given harmonic order a characteristic minimum of the calculated dipole amplitude and modulation of the phase appeared around a specific angle [131,132]. By comparison with a simple plane-wave model for the returning electron it was argued that this was due to interference between the dipole amplitudes from the two atomic centres in the molecule when they were separated by half the de Broglie wavelength  $\lambda_B$  of the returning electron. This idea is closely analogous to laser induced electron diffraction. The measurement of these recombination interference signatures for certain values of  $k$  will give almost directly the internuclear separation [132,134].

In some cases the conditions for interference correspond to the simple conditions for constructive and destructive two-point source interference [132,134]. They can be derived from Equation (8) by considering that the matrix element in this equation can also describe the recombination of the ejected electron on a molecular ion. In this case  $\psi_0$  is the HOMO and the major contribution to the integral in Equation (8) comes from the regions around the nuclei. Thus, by assuming (i) only the contributions from the volumes  $\Gamma_j$  around the nuclei and (ii) a constant value for both the ground state and the exponential function, we have

$$S(\Omega) \propto \Omega^4 |a(\omega)|^2 \left| \sum_j \psi_0(\mathbf{r}_j) \exp(i\mathbf{k}(\omega) \cdot \mathbf{r}_j) \right|^2 \delta(\Omega - \omega - I_p), \quad (9)$$

where the sum is over all the nuclei. The term  $\sum_j \psi_0(\mathbf{r}_j) \exp(i\mathbf{k}(\omega) \cdot \mathbf{r}_j)$  describes the interference between the contributions from the various atomic centres [132].

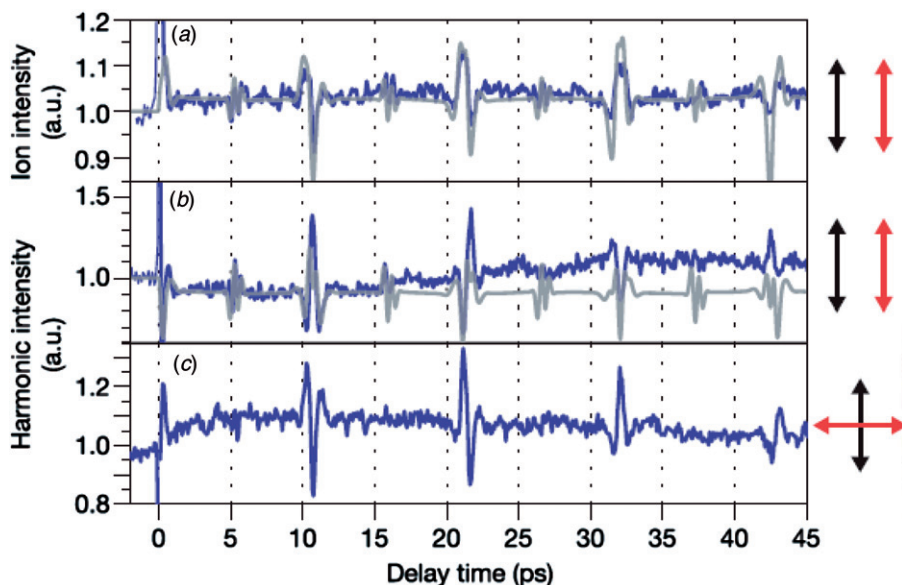


Figure 19. (a) The ion yield dominated by  $(\text{CO}_2)^+$  and (b)–(c) the 23rd harmonics from  $\text{CO}_2$  molecules as a function of pump–probe delay. The results of theoretical calculations are shown by grey curves. Reproduced with permission from T. Kanai et al. *Nature* **2005**, 435, 470. Copyright (2005), by Nature Publishing Group. (The colour version of this figure is included in the online version of the journal.)

For homonuclear diatomic molecules, we have to sum over the two positions  $\mathbf{r}_1$  and  $\mathbf{r}_2 = -\mathbf{r}_1$ . Furthermore, if the ground-state orbital has a particular symmetry ( $\psi_0(\mathbf{r}_1) = \psi_0(\mathbf{r}_2)$  or  $\psi_0(\mathbf{r}_1) = -\psi_0(\mathbf{r}_2)$ , i.e. so-called bonding or anti-bonding ground states) the relevant interference term is simply  $\exp(i\mathbf{k}(\omega) \cdot \mathbf{r}_1) \pm \exp(i\mathbf{k}(\omega) \cdot \mathbf{r}_2)$  (the upper and low sign is for symmetric and anti-symmetric HOMOs, respectively). For symmetric (anti-symmetric) HOMO, destructive (constructive) interference occurs when  $\mathbf{k} \cdot (\mathbf{r}_1 - \mathbf{r}_2) = (2m+1)\pi$  or, in terms of the projected internuclear distance  $R \cos \vartheta$  and the electron wavelength  $\lambda$ ,

$$R \cos \vartheta = (2m+1)\lambda/2, \quad m = 0, 1, 2, \dots \quad (10)$$

For symmetric (anti-symmetric) HOMO constructive (destructive) interference occurs for

$$R \cos \vartheta = m\lambda, \quad m = 0, 1, 2, \dots \quad (11)$$

This result describes the interference of two point emitters [132]. For multiple centred wavefunctions we can anticipate a more complex interference signature. The first observations of two centre interference, in the HHG spectrum of the  $\text{CO}_2$  molecule, were made in 2005 [133,134] (see Figures 19 and 20). In principle, this recombination interference signature can be obtained from a single alignment angle and in a few laser shots and so can lend itself readily to measurement of bond length changes in a pump–probe experiment. In fact the interpretation is not so simple, due to the difficulty of calculating HHG in molecules, but the experimental observation of two-centre interference and recent

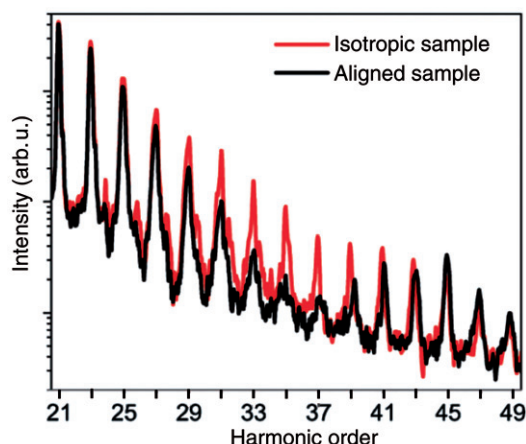


Figure 20. HHG spectra from  $\text{CO}_2$  measured for an isotropic sample (red line) and a non-adiabatically aligned sample (black line). The strong suppression of the signal for the aligned case extending from the 25th to 41st harmonics is an evidence of two-centre interference. Reproduced with permission from C. Vozzi et al. *Phys. Rev. Lett.* **2005**, 95, 153902. Copyright (2005) by the American Physical Society. (The colour version of this figure is included in the online version of the journal.)

progress in the theoretical treatment support the feasibility of these measurements.

### 6.3. Steps toward molecular imaging of more complex molecules

An extension of the approach described in the previous section to significantly more complex polyatomic

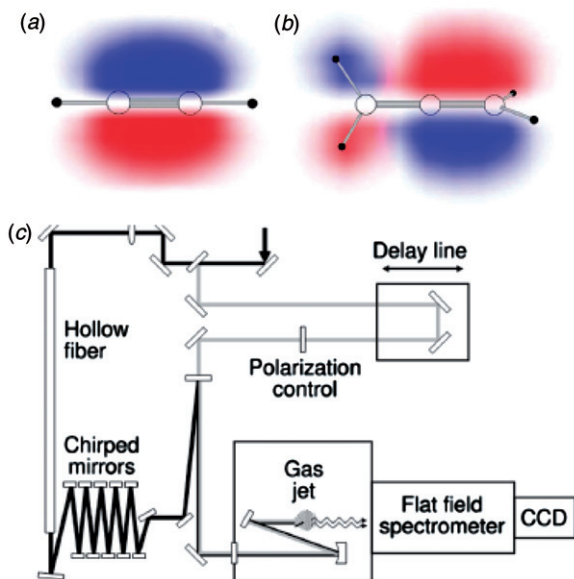


Figure 21. (a)–(b) Representation of one of the two degenerate orbitals comprising the HOMO in acetylene and allene, respectively. Different colours indicate different signs of the wave function. (c) Schematic layout of the experiment. The gray and black lines represent the aligning and harmonic generating beams, respectively. Reproduced with permission from R. Torres et al. *Phys. Rev. Lett.* **2007**, *98*, 203007. Copyright (2007) by the American Physical Society. (The colour version of this figure is included in the online version of the journal.)

molecules is reported in [139], where acetylene ( $\text{HC}\equiv\text{CH}$ ) and allene ( $\text{H}_2\text{C}=\text{C}=\text{CH}_2$ ) were considered. Both these organic molecules have HOMO dominated by the  $\pi_u$  orbital between the carbon atoms (see Figures 21(a) and (b)), though the allene molecule has additional contributions from C–H bonds.

The principle of the experimental setup is sketched in Figure 21(c). Basically, the generating beam (i.e. the laser beam which generates the harmonics) is spatially superimposed to the aligning beam after the latter is properly delayed in order to produce an aligning pulse which is correctly synchronised with the harmonic generating field. As a function of the delay, the signal of each harmonic shows a modulation resulting from the different degree of alignment which is similar to that reported in Figure 19 for  $\text{CO}_2$ . The regular revivals of the molecular axis alignment after the aligning pulse are a consequence of the regular space among the rotational energy levels which holds true for both linear (acetylene and carbon dioxide) and symmetric top (allene) molecules. For all harmonic orders in both molecules the modulation in the harmonic yield observed is anticorrelated with the degree of alignment, indicating a suppression in the harmonic yield when the molecules are preferentially aligned with their axes

parallel to the driving field polarisation. The maximum alignment occurs at the delays of 14.38 and 56.55 ps for acetylene and allene, respectively, whereas the opposite condition in which the molecules lie in the plane normal to the driving field polarisation is reached at 14.0 and 56.0 ps for acetylene and allene, respectively. Starting from these two alignment conditions the driving field polarisation can be rotated from  $0^\circ$  (parallel to the aligning beam polarisation) to  $90^\circ$  (normal to the aligning beam polarisation) to carry out a sort of tomography. The angular dependence of HHG yield normalised to the yield measured with isotropically distributed molecules (no aligning beam), is reported in Figure 22 for (a) acetylene and (b) allene. In both cases the left and right columns refer to the angular scan carried out at maximum alignment and anti-alignment, respectively. For all harmonic orders in both molecules, the harmonic yield is suppressed when the molecules are predominantly parallel to the field and increases with the angle. But in the proximity of the molecule at  $90^\circ$  with the electric field allene behaves differently from acetylene. Such a difference is well reproduced by the Lewenstein model [136] which is the starting point for Equation (8). The curves reported in both pictures are obtained with the HOMO corresponding to acetylene and allene, respectively, showing how HHG from these relatively simple molecules contains fingerprints of the molecular orbital from which the electron is freed.

#### 6.4. Probing attosecond dynamics by chirp encoded recollision (PACER)

High-order harmonic generation can be used as a tool to observe nuclear dynamics of the molecules occurring on a sub-fs time-scale through a recently developed technique termed PACER (probing attosecond dynamics by chirp encoded recollision) [8]. The principle of the technique is illustrated in Figure 23. Following the classical approach adopted within the so-called simple man model [125], harmonics are generated by electrons born into the continuum between  $\sim 1/20$ th of an optical cycle after the laser field maximum, which return to the ion approximately at the next zero of the field. The kinetic energy they can gain from the electric field depends on the precise emission and re-collision time instant, but from the classical point of view two possible trajectories allow the electron to gain the same energy. They differ in the elongation (distance from the nucleus) the electrons experience in their motion inasmuch as one is much shorter than the other [140]. These long trajectories can easily be filtered out from the spectrum by choosing an appropriate

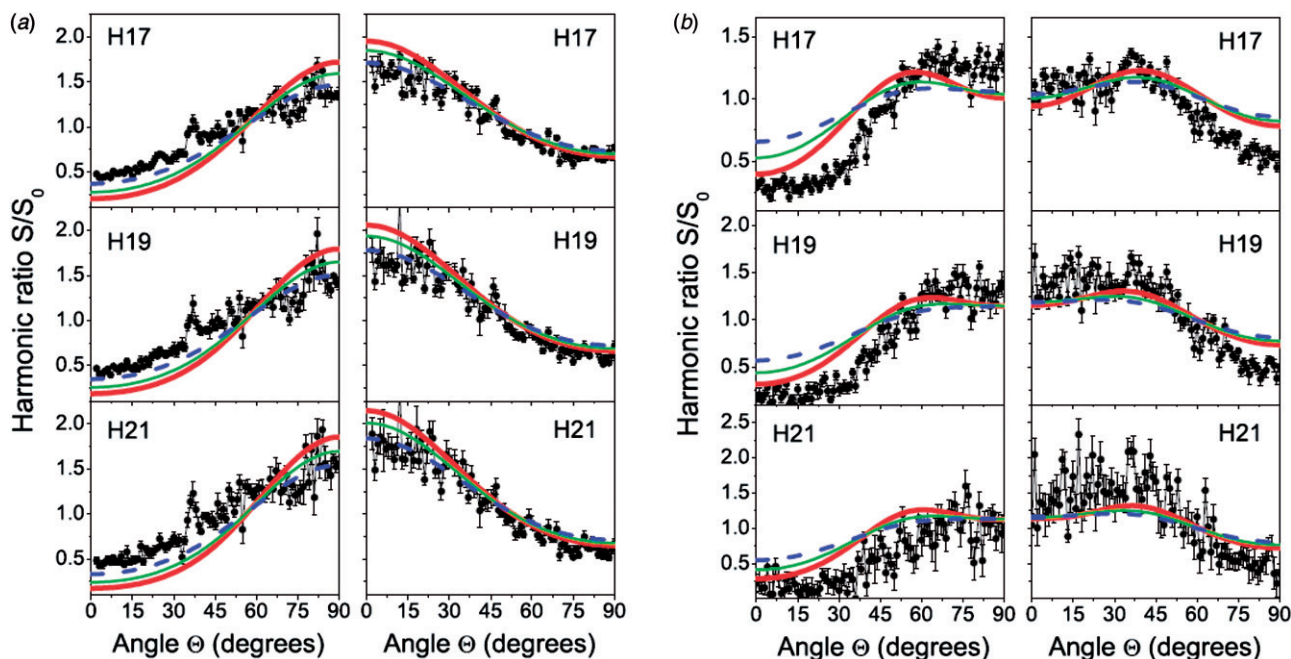


Figure 22. (a) Harmonic ratio between aligned and nonaligned acetylene molecules as a function of polarisation angle between aligning and driving beams, measured at the alignment peak ( $t_0 = 14.38$  ps) (left column) and the anti-alignment peak ( $t_0 = 14.0$  ps) (right column). The red thick solid, green thin solid and blue dashed curves show the calculated ratio in a sample at 20, 50, and 100 K, respectively. (b) The same as in (a) but for allene molecules for which the alignment peak is at  $t_0 = 56.55$  ps (left column) and the anti-alignment peak at  $t_0 = 56.0$  ps (right column). Reproduced with permission from R. Torres et al. *Phys. Rev. Lett.* **2007**, 98, 203007. Copyright (2007) by the American Physical Society. (The colour version of this figure is included in the online version of the journal.)

position of the laser focus with respect to the gas jet, thus yielding a one-to-one mapping between delay and photon frequency (Figure 23) because each of these short trajectories is associated with an electron returning to the parent ion at a different delay time  $\Delta t$  with a proper electron kinetic energy [82]. Thus, the chirped nature of the recolliding electron wavepacket (Figure 23) can be exploited to achieve a sub-femtosecond temporal resolution in a variety of pump-probe schemes by analysing the single harmonic spectrum. As an example, due to the dependence of the harmonic signal on the changes in the nuclear part of the wave function  $\chi(R, t)$ , it is possible to probe the nuclear motion during the excursion time of the electron  $\tau$ . This is because the harmonic signal in a molecule is approximately proportional to the squared modulus of the nuclear autocorrelation function [141]  $c(t) = \int \chi(R, 0) \chi(R, \tau) d\tau$  (overlap between the initial and final nuclear parts of the molecular wave function) which decreases the more the nuclei move in the small time interval. Thus, the entire HHG spectrum is determined by the squared modulus of  $c(t)$  and of the remaining parts of the transition dipole moment that do not depend on the nuclear motion (see Equation (8)).

Marangos and co-workers [8] implemented this method by observing the ratio of the harmonic spectra generated in gaseous  $H_2$  and  $D_2$ , or  $CH_4$  and  $CD_4$ . Since in isotopes the electronic states are very similar, the variation in HHG spectra can only be associated with differing nuclear dynamics, which can be retrieved by the ratio between harmonic peak intensities for different isotopes with a resolution of the order of 100 as over a range of  $\sim 1$  fs for laser light of  $\sim 800$  nm wavelength. In Figure 24(a) the ratio of harmonics peak intensities for  $D_2$  and  $H_2$  is reported versus the recollision time (black). Also reported is the control ratio of two harmonic spectra from  $H_2$  taken separately (red) which is as expected. The blue curve represents the theoretical ratio worked out by Equation (8) and the autocorrelation function  $c(t)$ . The agreement with the experiment allows one to retrieve the nuclear dynamics and this is shown in Figure 24(b) for  $(H_2)^+$  and  $(D_2)^+$ , where the red lines are the results of the application of a genetic algorithm [141] and converge to the blue lines which represent the exact calculation for  $H_2$  (dashed) and  $D_2$  (solid), respectively, in a Born-Oppenheimer potential. It is worth to mention that such a method is able to retrieve not only the mean value of the internuclear distance as

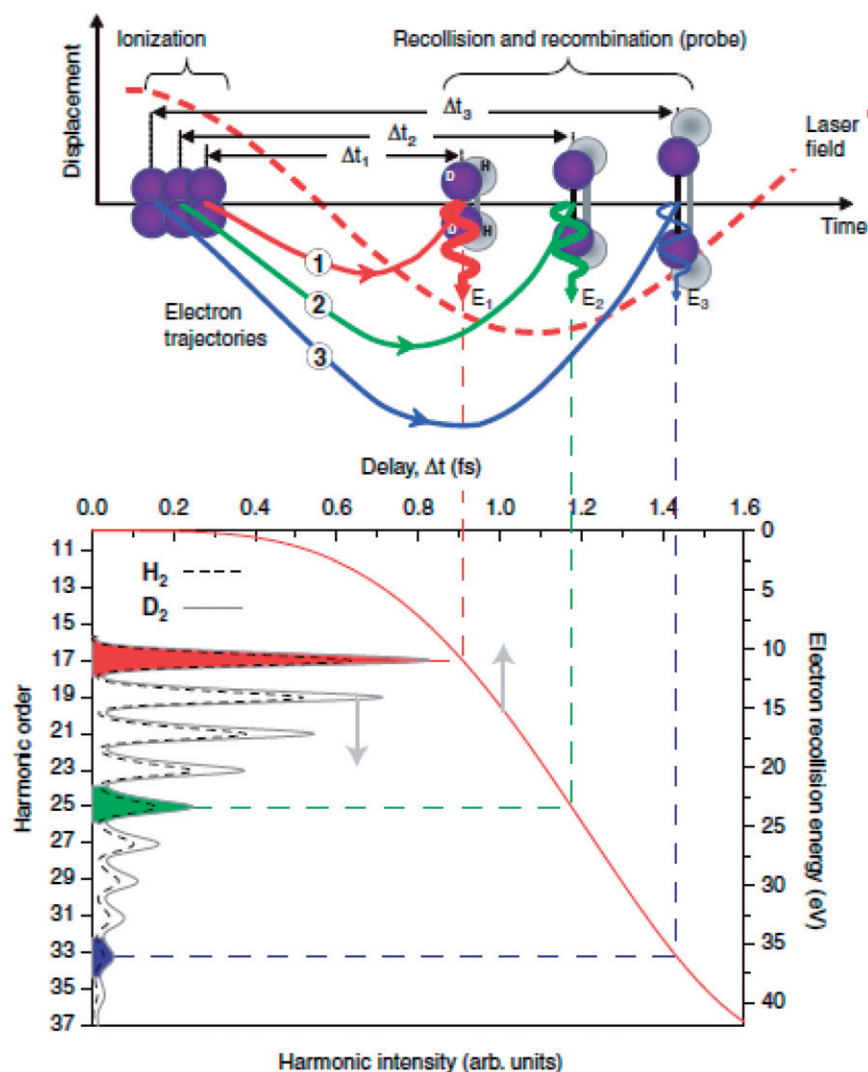


Figure 23. Encoding of nuclear dynamics within harmonic spectra. The trajectory of the ionised electron differs depending on the exact time of ionisation. Three possible electron trajectories labelled 1, 2, and 3 are shown, which recollide with the molecular ion after delays  $\Delta t_1$ ,  $\Delta t_2$ , and  $\Delta t_3$ , with increasing kinetic energy  $E_1$ ,  $E_2$ , and  $E_3$ , resulting in the emission of increasingly higher frequency photons after recombination (shown as the 17th, 25th, and 33rd harmonics for the purpose of this illustration). Reproduced with permission from S. Baker et al. *Science* **2006**, 312, 424. Copyright (2006) by AAAS. (The colour version of this figure is included in the online version of the journal.)

a function of time, but also the shape of the time-dependent wave packet.

## 7. Discussion

### 7.1. State of the art

In Table 1 we attempt to capture the critical capabilities of the major techniques covered in this review for ultrafast structural dynamic measurements. The table content reflects the current state of the art, but includes the likely performance of X-ray techniques enabled by the availability of hard X-ray FELs which are just becoming available (i.e. LCLS) at the time of writing.

Likewise for UED we extrapolate to the near future performance of optimised non-relativistic and relativistic electron pulse sources. For all of the methods, excepting causality inverted IXS and the intramolecular rearrangements caused by ionisation probed by HHG, the time resolution comes from a pump-probe measurement. It is not specified how this might be done and a full discussion of the physics and technology of the pump step is outside the scope of this review.

In the first two columns the limits to temporal and spatial resolution are given. It is the pulse duration that limits the ultimate temporal resolution in X-ray spectroscopy, X-ray diffraction and electron diffraction, but the properties of the pump and the pump-probe

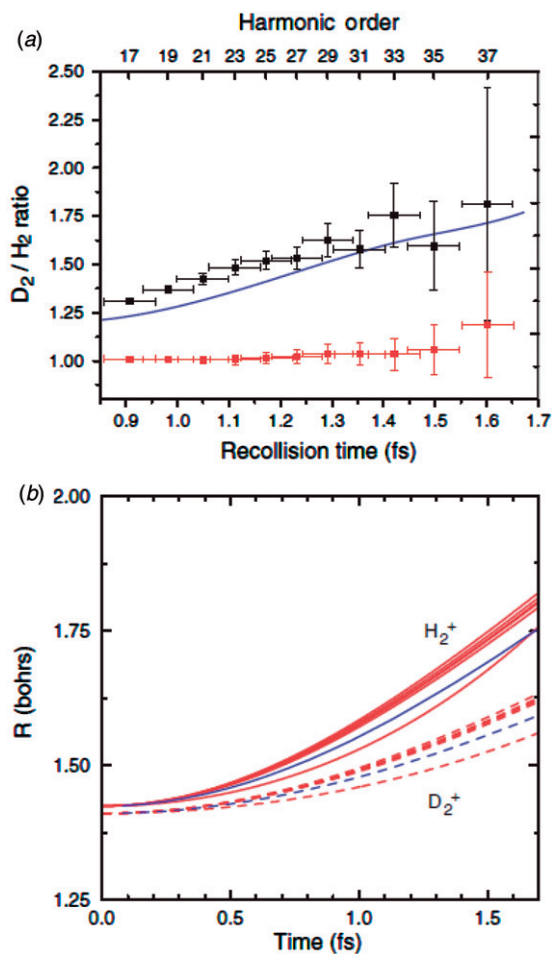


Figure 24. (a) Ratio of harmonic peak intensities for  $D_2$  and  $H_2$  (black). The control ratio of two harmonic spectra from  $H_2$  taken separately is also shown (red) and is seen to be unity for all harmonic orders, as expected. The blue line is a calculation of harmonic ratio (see [8]). (b) The nuclear motion reconstructed from the experimental data by multiple runs of a genetic algorithm (red curves) converges closely to the exact result (blue curves) calculated using the exact Born–Oppenheimer potentials for  $H_2$  and  $D_2$ . Reproduced with permission from S. Baker et al. *Science* **2006**, 312, 424. Copyright (2006) by AAAS. (The colour version of this figure is included in the online version of the journal.)

synchronisation that will also determine the best temporal resolution in any real measurement. Thus comparing the performance of a FEL in SASE, seeded or one of the sub-femtosecond operating modes (e.g. single spike) it is important to factor in the temporal jitter that may well mean a seeded FEL offers measurements with far superior temporal resolution even than a single-spike operation [NLS Science Case and ODR, July 2009]. For laser-based measurements relying on HHG production, strong field ionisation or electron recollision, the time resolution can be in the sub-optical cycle region. The spatial resolution limits

of the already proven structural methods, e.g. involving Bragg diffraction of electrons or X-rays, is already known to be exceptionally good (a few % of the interatomic distance in many cases). For some of the newer techniques (IXS or laser based) this is not yet fully quantified, moreover the laser techniques are probing the valence electron wavefunctions rather than the atomic arrangement, with the exception of laser induced electron diffraction where it is anticipated that the scattering from core electrons and nuclei will localise the structural information.

The actual method by which the signal from the probe is recorded is listed as it gives some indications of the data acquisition speed. So for instance although HHG imaging and HHG induced photoelectrons may in principle give the same information the measurement in the case of the former is essentially single shot whilst for the latter the photoelectron angular distribution may have to be accumulated over many shots at each XUV energy, and the XUV energy scanned, to obtain the same data. The most striking advantage of the ‘traditional’ structural methods are their superior spatial resolution and the range of sample states to which they can be applied (solid, liquid and gas) due to the high penetration of harder X-rays. In contrast the laser-based techniques have temporal resolution advantages as often the measurement has sub-optical cycle capability, but are restricted to gas phase or surface due to the lack of penetration of the optical field. An extension of laser induced tunnelling to look at spatially dependent breakdown may lift this restriction at least for transparent dielectrics.

All of the pump–probe methods are ideally suited to capture transient species (i.e. those that may only exist for a short time following the pump). IXS being a time-integrated technique lacks this although it is uniquely appropriate to probe the ultrafast electron dynamics of matter within the static structure. A similar comment can extend to HHG imaging (e.g. PACER measurements) where the very fast dynamics triggered by the strong field are probed by the HHG, but in other modes HHG can be incorporated into a more conventional pump–probe scenario that will capture transient species. Reliable reconstruction of the structural dynamics is a key attribute. The methods to achieve this for X-ray spectroscopy, X-ray diffraction and electron diffraction are all firmly established in the static regime and the extrapolation to the time-resolved domain is trivial. The laser-based methods, relying on the interaction of the matter with a strong field as they do, require quantitative theoretical models to ensure reliable extraction of the structural dynamics, at least whilst the general principles are being established. It is hoped that in future it will be possible, once the robust features and general principles are

Table 1. Summary of the main techniques reviewed.

Probe	Temporal resolution	Spatial resolution	Detection method	Sample type	Capture transient	Reconstruction of structural dynamics
XAS	Limited by X-ray pulse & pump-probe synchrony (~20 fs FEL)	<0.1 Å atomic arrangement	X-ray absorption Spectra	Solids, liquids, gases, homogeneous, heterogeneous	Yes	Established EXAFS methods
IXS	Energy transfer range ~20 as	Momentum transfer range ~1 Å	Inelastic $E$ & $k$ resolved measurement	Homogeneous solids & liquids	No	Causality inverted reconstruction – yet to be generalised
X-ray diffraction	Limited by X-ray pulse & pump-probe synchrony (~20 fs FEL)	<0.1 Å atomic arrangement	X-ray scatter pattern	Solids & liquids non-periodic for CDI	Yes	Bragg diffraction theory Or Numerical methods (CDI)
Electron diffraction	>100 fs non-re	<0.1 Å atomic arrangement	Electron scatter distribution	Solids, liquids, gases	Yes	Bragg diffraction theory
Laser ionisation	<1 fs Sub-optical cycle	~1 Å electron wf	Angle resolved ion rate	Gas phase molecules	Yes	Quantitative strong field theory
CEI	~5 fs laser pulse duration	~1 Å	Ion fragment Pattern	Gas phase molecules	Yes	Quantitative laser molecule interaction theory
HHG ionisation	<1 fs attosecond pulse duration	~1 Å electron wf	Electron momentum in presence of IR field	Gas phase molecules	Yes	Quantitative molecule X-ray interaction theory
HHG imaging	<1 fs Sub-optical cycle	~1 Å electron wf	HHG spectra for defined molecule orientation	Gas phase molecule (surfaces?)	Yes	Quantitative strong field theory
Laser driven electron diffraction	<1 fs Sub-optical cycle	<1 Å Atomic arrangement	Electrons rescattered from orientated molecules	Molecular gases surfaces?	Yes	Theory of electron diffraction in a strong field

identified, to circumvent the need for a detailed and specific theoretical treatment for each new system probed. The hope for HHG imaging is to establish and then apply some general principles already verified in specific examples such as is done in EXAFS.

### 7.2. Challenges and limits

The table of the previous section presents the close to state of the art for the various techniques discussed previously; the question arises as to what are the limits of these methods. Improvements of light sources are the most obvious way to improve the temporal resolution of the X-ray pulsed techniques; but this must be accompanied with matching temporal synchronisation for the pump step in pump-probe methods. Current FELs are limited to SASE mode operation and this results in significant temporal jitter with respect to external lasers; realistically to  $\pm 50$  fs. Future seeded FELs may achieve better temporal synchronisation to the few femtosecond level that will permit the full exploitation of X-ray pulse durations down to 10 fs in X-ray diffraction and X-ray absorption techniques for sufficiently thin samples. Shorter pulsed FEL operation (to  $< 1$  fs) has been posited by a variety of routes, low bunch charge operation such that the X-ray lasing occurs on a single temporal spike even in SASE mode is the method closest to realisation. This again leads to jitter although if the measurement can work from an X-ray trigger from the same pulse a simple split-and-delay method might be implemented to achieve the sub-femtosecond temporal resolution. Otherwise sub-fs time-resolved pump-probe X-ray methods must await the arrival of fully laser synchronised sub-fs X-ray FEL methods to achieve attosecond domain measurement.

In any event pump pulse durations are limited by the carrier frequency to something longer than an optical cycle, e.g. a 10 THz carrier can support a pulse only longer than 100 fs. This means that no sub-femtosecond resolved pump-probe experiments are possible except for pump pulses in the ultra-violet region of the spectrum or at shorter wavelength. Methods such as HHG imaging, attosecond streaking and IXS are attractive as they circumvent the need to contrive two independently generated sub-fs pulses at different frequencies. If slower dynamics are being probed there is still the need to ensure that the pump pulse has sufficient power to ensure a significant degree of excitation of the mode of interest. There remains the need to further develop pump pulses in the far-IR – THz region.

The chief limit that can be identified for laser-based sources is the fact that due to the need to expose the

sample to high intensity and/or XUV wavelength short pulses the methods are confined to gas phase samples or the first few atomic layers of a surface. Whilst techniques for introducing large molecules into gas phase environments have advanced (e.g. ablation, MALDI) this still precludes the application to measure ultra-fast structural dynamics in solid and liquid phase. There remain a wealth of problems of structural dynamics, many of fundamental importance to our understanding of questions of charge and energy flow and geometry change in physical and chemical changes, that can be answered by examining gas phase molecules, surfaces and nanostructures.

### 7.3. Future prospects

It is anticipated that the biggest single impact upon the field will be from the soft to hard X-ray FELs that are now becoming available or are being planned around the world. These devices offer a remarkable combination of exceptionally short pulse durations ( $\sim 10$  fs), X-ray wavelengths and enormous peak and average brightness. The fact that they can be closely synchronised to auxiliary lasers (to incredible accuracy if seeding or laser modulation of the electron beam are implemented) opens the prospects for a revolutionary change in the scope of time-resolved X-ray measurement. Given that harder X-rays can penetrate even into solid samples the combined techniques (X-ray spectroscopy, photoelectron emission, X-ray scattering) potentially provide an almost universal tool for ultra-fast structural imaging.

Nevertheless, the advances promised in pulsed electron sources for UED, especially the ideas for relativistic beams and 4D electron diffraction, are also likely to establish an important niche especially for the study of surfaces and gas phase systems. Likewise the laser-based methods – attosecond XUV pulses, HHG imaging, laser induced electron diffraction – although confined to gas phase molecules, surfaces and clusters can provide unprecedented temporal resolution matching the characteristic timescales of electron dynamics in matter and so will advance our knowledge of the fastest fundamental electronic events in matter.

### References

- [1] Rousse, A.; Rischel, C.; Gauthier, G.C. *Rev. Mod. Phys.* **2001**, *73*, 17–31.
- [2] Bressler, C.; Chergui, M. *Chem. Rev.* **2004**, *104*, 1781–1812.
- [3] Khan, S. *J. Mod. Opt.* **2008**, *55*, 3469–3512.
- [4] Siwick, B.J.; Dwyer, J.R.; Jordan, R.E.; Miller, R.J.D. *Science* **2003**, *302*, 1382–1385.

- [5] Corkum, P.B.; Krausz, F. *Nat. Phys.* **2007**, *3*, 381–387.
- [6] Eckle, P.; Pfeiffer, A.N.; Cirelli, C.; Staudte, A.; Dörner, R.; Müller, H.G.; Büttiker, M.; Keller, U. *Science* **2008**, *322*, 1525–1529.
- [7] Itatani, J.; Levesque, J.; Zeidler, D.; Niikura, H.; Pépin, H.; Kieffer, J.C.; Corkum, P.B.; Villeneuve, D.M. *Nature* **2004**, *432*, 867–871.
- [8] Baker, S.; Robinson, J.S.; Haworth, C.A.; Teng, H.; Smith, R.A.; Chirila, C.C.; Lein, M.; Tisch, J.W.G.; Marangos, J.P. *Science* **2006**, *312*, 424–427.
- [9] Marangos, J.P.; Baker, S.; Kajumba, N.; Robinson, J.S.; Tisch, J.W.G.; Torres, R. *Phys. Chem. Chem. Phys.* **2008**, *10*, 35–48.
- [10] Meckel, M.; Comtois, D.; Zeidler, D.; Staudte, A.; Pavičič, D.; Bandulet, H.C.; Pépin, H.; Kieffer, J.C.; Dörner, R.; Villeneuve, D.M.; Corkum, P.B. *Science* **2008**, *320*, 1478–1482.
- [11] Blanchet, V.; Zgierski, M.Z.; Seideman, T.; Stolow, A. *Nature* **1999**, *401*, 52–54.
- [12] Remetter, T.; Johnsson, P.; Mauritsson, J.; Varjú, K.; Ni, Y.; Lépine, F.; Gustafsson, E.; Kling, M.; Khan, J.; López-Martens, R.; Schafer, K.J.; Vrakking, M.J.J.; L’Huillier, A. *Nat. Phys.* **2006**, *2*, 323–326.
- [13] Vager, Z.; Naaman, R.; Kanter, E.P. *Science* **1989**, *244*, 426–431.
- [14] Codling, K.; Frasninski, L.J. *J. Phys. B: At. Mol. Opt. Phys.* **1993**, *26*, 783–809.
- [15] Goulielmakis, E.; Uiberacker, M.; Kienberger, R.; Baltuska, A.; Yakovlev, V.; Scrinzi, A.; Westerwalbesloh, Th.; Kleineberg, U.; Heinzmann, U.; Drescher, M.; Krausz, F. *Science* **2004**, *302*, 1267–1269.
- [16] Uiberacker, M.; Uphues, T.; Schultze, M.; Verhoef, A.J.; Yakovlev, V.; Kling, M.F.; Rauschenberger, J.; Kabachnik, N.M.; Schröder, H.; Lezius, M.; Kompa, K.L.; Müller, H.-G.; Vrakking, M.J.J.; Hendel, S.; Kleineberg, U.; Heinzmann, U.; Drescher, M.; Krausz, F. *Nature* **2007**, *446*, 627–632.
- [17] Cavalieri, A.L.; Müller, N.; Uphues, Th.; Yakovlev, V.S.; Baltuška, A.; Horvath, B.; Schmidt, B.; Blümel, L.; Holzwarth, R.; Hendel, S.; Drescher, M.; Kleineberg, U.; Echenique, P.M.; Kienberger, R.; Krausz, F.; Heinzmann, U. *Nature* **2007**, *449*, 1029–1032.
- [18] Frühling, U.; Wielland, M.; Gensch, M.; Gebert, T.; Schütte, B.; Krikunova, M.; Kalms, R.; Budzyn, F.; Grimm, O.; Rossbach, J.; Plönjes, E.; Drescher, M. *Nat. Photon.* **2009**, *3*, 523–528.
- [19] Judson, R.S.; Rabitz, H. *Phys. Rev. Lett.* **1992**, *68*, 1500–1503.
- [20] Assion, A.; Baumert, T.; Bergt, M.; Brixner, T.; Kiefer, B.; Seyfried, V.; Strehle, M.; Gerber, G. *Science* **1998**, *282*, 919–922.
- [21] Rehr, J.J.; Albers, R.C. *Rev. Mod. Phys.* **2000**, *72*, 621–654.
- [22] Bruthwiller, P.A.; Karis, O.; Martensson, N. *Rev. Mod. Phys.* **2002**, *74*, 703–740.
- [23] Raksi, F.; Wilson, K.R.; Jiang, Z.; Ikhlef, A.; Côté, C.Y.; Kieffer, J.-C. *J. Chem. Phys.* **1996**, *104*, 6066–6069.
- [24] Gawelda, W.; Pham, V.-T.; Benfatto, M.; Zaushtsyn, Y.; Kaiser, M.; Grolimund, D.; Johnson, S.L.; Abela, R.; Hauser, A.; Bressler, Ch.; Chergui, M. *Phys. Rev. Lett.* **2007**, *98*, 057401.
- [25] Johnson, S.L.; Heimann, P.A.; MacPhee, A.G.; Lindenberg, A.M.; Monteiro, O.R.; Chang, Z.; Lee, R.W.; Falcone, R.W. *Phys. Rev. Lett.* **2005**, *94*, 057407.
- [26] Bressler, Ch.; Milne, C.; Pham, V.-T.; EINahhas, A.; van der Veen, R.M.; Gawelda, W.; Johnson, S.; Beaud, P.; Grolimund, D.; Kaiser, M.; Borca, C.N.; Ingold, G.; Abela, R.; Chergui, M. *Science* **2009**, *323*, 489–492.
- [27] New Light Source Report ‘Science Case and Outline Facility Design’, Science and Technology Facility Council, Swindon, UK, July 2009.
- [28] Bragg, W.L. *Proc. Cambridge Philos. Soc.* **1913**, *17*, 43–57.
- [29] Watson, J.D.; Crick, F.H.C. *Nature* **1953**, *171*, 737–738.
- [30] Rischel, Ch.; Rouse, A.; Uschmann, I.; Albouy, P.-A.; Geindre, J.-P.; Audebert, P.; Gauthier, J.-C.; Fröster, E.; Martin, J.-L.; Antonetti, A. *Nature* **1997**, *390*, 490–492.
- [31] Chin, A.H.; Schoenlein, R.W.; Glover, T.E.; Balling, P.; Leemans, W.P.; Shank, C.V. *Phys. Rev. Lett.* **1999**, *83*, 336–339.
- [32] Siders, C.W.; Cavalleri, A.; Sokolowski-Tinten, K.; Tóth, Cs.; Guo, T.; Kammler, M.; Horn von Hoegen, M.; Wilson, K.R.; von der Linde, D.; Barty, C.P.J. *Science* **1999**, *286*, 1340–1342.
- [33] Rose-Petrucci, C.R.; Jimenez, R.; Guo, T.; Cavalleri, A.; Siders, C.W.; Raksi, F.; Squier, J.A.; Walker, B.C.; Wilson, K.R.; Barty, C.P.J. *Nature* **1999**, *398*, 310–312.
- [34] Lindenberg, A.M.; Kang, I.; Johnson, S.L.; Missalla, T.; Heimann, P.A.; Chang, Z.; Larsson, J.; Bucksbaum, P.H.; Kapteyn, H.C.; Padmore, H.A.; Lee, R.W.; Wark, S.; Facone, R.W. *Phys. Rev. Lett.* **2000**, *84*, 111–114.
- [35] Schotte, F.; Manho, L.; Jackson, T.A.; Smirnov, A.V.; Soman, J.; Olson, J.S.; Phillips, G.N.; Wulff, M.; Anfinrud, P.A. *Science* **2003**, *300*, 1944–1947.
- [36] Neutze, R.; Huidt, G.; Hajdu, J.; van der Spoel, D. *Radiat. Phys. Chem.* **2004**, *71*, 905–916.
- [37] Sayre, D. *Acta Crystallogr.* **1952**, *5*, 843–843.
- [38] Feinup, J.R. *Appl. Opt.* **1982**, *21*, 2758–2769.
- [39] Miao, J.; Charalambous, P.; Kirz, J.; Sayre, D. *Nature* **1999**, *400*, 342–344.
- [40] Chapman, H.N.; Barty, A.; Bogan, M.J.; Boutet, S.; Frank, M.; Hau-Riege, S.P.; Marchesini, S.; Woods, B.W.; Bajt, S.; Benner, W.H.; London, R.A.; Plönjes, E.; Kuhlmann, M.; Treusch, R.; Düsterer, S.; Tschentscher, T.; Schneider, J.R.; Spiller, E.; Möller, T.; Bostedt, C.; Hoener, M.; Shapiro, D.A.; Hodgson, K.O.; van der Spoel, D.; Burmeister, F.; Bergh, M.; Caleman, C.; Huidt, G.; Seibert, M.M.; Maia, F.R.N.C.; Lee, R.W.; Szöke, A.; Timneanu, N.; Hajdu, J. *Nat. Phys.* **2006**, *2*, 839–843.
- [41] Barty, A.; Boutet, S.; Bogan, M.J.; Hau-Riege, S.; Marchesini, S.; Sokolowski-Tinten, K.; Stojanovic, N.; Tobey, R.; Ehrke, H.; Cavalleri, A.; Düsterer, S.; Frank, M.; Bajt, S.; Woods, B.W.; Seibert, M.M.; Hajdu, J.; Treusch, R.; Chapman, H.N. *Nat. Photon.* **2008**, *2*, 415–419.
- [42] Busse, G.; Tschentscher, T.; Plech, A.; Wulff, M.; Frederichs, B.; Techert, S. *Faraday Discuss.* **2003**, *122*, 105–117.

- [43] Lindenberg, A.M.; Larsson, J.; Sokolowski-Tinten, K.; Gaffney, K.J.; Blome, C.; Synnergren, O.; Sheppard, J.; Coleman, C.; MacPhee, A.G.; Weinstein, D.; Lowney, D.P.; Allison, T.K.; Matthews, T.; Falcone, R.W.; Cavalieri, A.L.; Fritz, D.M.; Lee, S.H.; Bucksbaum, P.H.; Reis, D.A.; Rudati, J.; Fuoss, P.H.; Kao, C.C.; Siddons, D.P.; Pahl, R.; Als-Nielsen, J.; Duesterer, S.; Ischebeck, R.; Schlarb, H.; Schulte-Schrepping, H.; Tschentscher, Th.; Schneider, J.; von der Linde, D.; Hignette, O.; Sette, F.; Chapman, H.N.; Lee, R.W.; Hansen, T.N.; Teichert, S.; Wark, J.S.; Bergh, M.; Huldt, G.; van der Spoel, D.; Timneanu, N.; Hajdu, J.; Akre, R.A.; Bong, E.; Krejčík, P.; Arthur, J.; Brennan, S.; Luening, K.; Hastings, J.B. *Science* **2005**, *308*, 392–395.
- [44] Abbamonte, P.; Finkelstein, K.D.; Collins, M.D.; Gruner, S.M. *Phys. Rev. Lett.* **2004**, *92*, 237401.
- [45] Abbamonte, P.; Graber, T.; Reed, J.P.; Smadici, S.; Yeh, C.-L.; Shukla, A.; Rueff, J.-P.; Ku, W. *Proc. Natl. Acad. Sci. USA* **2008**, *105*, 12159–12163.
- [46] Thomson, G.P. *Nature* **1927**, *120*, 802–802.
- [47] Davisson, C.; Germer, L.H. *Nature* **1927**, *119*, 558–560.
- [48] Ihee, H.; Lobastov, V.A.; Gomez, U.M.; Goodson, B.M.; Srinivasan, R.; Ruan, C.-Y.; Zewail, A.H. *Science* **2001**, *291*, 458–462.
- [49] Williamson, J.C.; Cao, J.; Ihee, H.; Frey, H.; Zewail, A.H. *Nature* **1997**, *386*, 159–162.
- [50] Siwick, B.J.; Dwyer, J.R.; Jordan, R.E.; Miller, R.J.D. *J. Appl. Phys.* **2002**, *92*, 1643–1648.
- [51] Hastings, J.N.; Rudakov, J.B.; Dowell, F.M.; Schmerge, J.F.; Cardoza, J.D.; Castro, J.M.; Gierman, S.M.; Loos, H.; Weber, P.M. *Appl. Phys. Lett.* **2006**, *89*, 184109.
- [52] Baum, P.; Zewail, A.H. *Proc. Natl. Acad. Sci. USA* **2007**, *104*, 18409–18414.
- [53] Hilbert, S.A.; Uiterwaal, C.; Barwick, B.; Batelaan, H.; Zewail, A.H. *Proc. Natl. Acad. Sci. USA* **2009**, *106*, 10558–10563.
- [54] Posthumus, J.H. *Rep. Prog. Phys.* **2004**, *67*, 623–665.
- [55] Légaré, F.; Lee, K.F.; Litvinyuk, I.V.; Dooley, P.W.; Wesolowski, S.S.; Bunker, P.R.; Dombi, P.; Krausz, F.; Bandrauk, D.; Villeneuve, D.M.; Corkum, P.B. *Phys. Rev. A* **2005**, *71*, 013415.
- [56] Cornaggia, C. *Laser Phys.* **2009**, *19*, 1660–1670.
- [57] Frasinski, L.J.; Codling, K.; Hatherly, P.A. *Science* **1989**, *246*, 1029–1031.
- [58] Kanter, E.P.; Cooney, P.J.; Gemmell, D.S.; Groeneveld, K.-O.; Pietsch, W.J.; Ratkowski, A.J.; Vager, Z.; Zabransky, B.J. *Phys. Rev. A* **1979**, *20*, 834–854.
- [59] Hishikawa, A.; Matsuda, A.; Fushitani, M.; Takahashi, E.J. *Phys. Rev. Lett.* **2007**, *99*, 258302.
- [60] Zewail, A.H. *Ann. Rev. Phys. Chem.* **2006**, *57*, 65–103.
- [61] Reckenthaeler, P.; Centurion, M.; Fuss, W.; Trushin, S.A.; Krausz, F.; Fill, E.E. *Phys. Rev. Lett.* **2009**, *102*, 213001.
- [62] Nie, S.H.; Wang, X.; Park, H.; Clinite, R.; Cao, J. *Phys. Rev. Lett.* **2006**, *96*, 025901.
- [63] Fill, E.E.; Veisz, L.; Apolonski, A.; Krausz, F. *New J. Phys.* **2006**, *8*, 272.
- [64] Zuo, T.; Bandrauk, A.D.; Corkum, P.B. *Chem. Phys. Lett.* **1996**, *259*, 313–320.
- [65] Niikura, H.; Légaré, F.; Hasbani, R.; Ivanov, M.Y.; Villeneuve, D.M.; Corkum, P.B. *Nature* **2002**, *417*, 917–922.
- [66] Dörner, R.; Mergel, V.; Jagutzki, O.; Spielberger, L.; Ullrich, J.; Moshhammer, R.; Schmidt-Böcking, H. *Phys. Rep.* **2000**, *330*, 95–192.
- [67] McPherson, A.; Gibson, G.; Jara, H.; Johann, U.; Luk, T.S.; McIntyre, I.A.; Boyer, K.; Rhodes, C.K. *J. Opt. Soc. Am. B* **1987**, *4*, 595–601.
- [68] Ferray, M.; L’Huillier, A.; Li, X.F.; Lompré, L.A.; Mainfray, G.; Manus, C. *J. Phys. B* **1988**, *21*, L31–L37.
- [69] Nabekawa, Y.; Shimizu, T.; Furukawa, Y.; Takahashi, E.J.; Midorikawa, K. *Phys. Rev. Lett.* **2009**, *102*, 213904.
- [70] Krausz, F.; Ivanov, M. *Rev. Mod. Phys.* **2009**, *81*, 163–234.
- [71] Nisoli, M.; Sansone, G. *Prog. Quantum Electron.* **2009**, *33*, 17–59.
- [72] Niikura, H.; Légaré, F.; Hasbani, R.; Ivanov, M.Y.; Villeneuve, D.M.; Corkum, P.B. *Nature* **2003**, *421*, 826–829.
- [73] Varjú, K.; Mairesse, Y.; Agostini, P.; Breger, P.; Carré, B.; Frasinski, L.J.; Gustafsson, E.; Johnsson, P.; Mauritsson, H.; Merdji, H.; Monchicourt, P.; L’Huillier, A.; Salières, P. *Phys. Rev. Lett.* **2005**, *95*, 243901.
- [74] Huo, Y.; Zeng, Z.; Leng, Y.; Li, R.; Xu, Z.; Guo, C.; Sun, Z.; Rhee, Y. *Opt. Lett.* **2005**, *30*, 564–566.
- [75] Paulus, G.G.; Grasbon, F.; Walther, H.; Villoresi, P.; Nisoli, M.; Stagira, S.; Priori, E.; De Silvestri, S. *Nature* **2001**, *414*, 182–184.
- [76] Jones, D.J.; Diddams, S.A.; Ranka, J.K.; Stentz, A.; Windeler, R.S.; Hall, J.L.; Cundiff, S.T. *Science* **2000**, *288*, 635–639.
- [77] Baltuška, A.; Fuji, T.; Kobayashi, T. *Opt. Lett.* **2002**, *27*, 1241–1243.
- [78] Baltuška, A.; Udem, Th.; Uiberacker, M.; Hentschel, M.; Goulielmakis, E.; Gohle, Ch.; Holzwarth, R.; Yakovlev, V.S.; Scrinzi, A.; Hänsch, T.W.; Krausz, F. *Nature* **2003**, *421*, 611–615.
- [79] Sola, I.J.; Mével, E.; Elouga, L.; Constant, E.; Strelkov, V.; Poletto, L.; Villoresi, P.; Benedetti, E.; Caumes, J.-P.; Stagira, S.; Vozzi, C.; Sansone, G.; Nisoli, M. *Nat. Phys.* **2006**, *2*, 319–322.
- [80] Sansone, G.; Benedetti, E.; Calegari, F.; Vozzi, C.; Avaldi, L.; Flammini, R.; Poletto, L.; Villoresi, P.; Altucci, C.; Velotta, R.; Stagira, S.; De Silvestri, S.; Nisoli, M. *Science* **2006**, *314*, 443–445.
- [81] Mairesse, Y.; Quéré, F. *Phys. Rev. A* **2005**, *71*, 011401(R).
- [82] Mairesse, Y.; de Bohan, A.; Frasinsky, L.J.; Merdji, H.; Dinu, L.C.; Monchicourt, P.; Breger, P.; Kovacev, M.; Taïeb, R.; Carré, B.; Muller, H.G.; Agostini, P.; Salières, P. *Science* **2003**, *302*, 1540–1543.
- [83] Wonisch, A.; Westerwalbesloh, Th.; Hachmann, W.; Kabachnik, N.; Kleineberg, U.; Heinzmann, U. *This Solid Films* **2004**, *473*, 464–465.
- [84] Morlens, A.; Balcou, P.; Zeitoun, P.; Valentin, C.; Laude, V.; Kazamias, S. *Opt. Lett.* **2005**, *30*, 1554–1556.
- [85] Wonisch, A.; Neuhäusler, U.; Kabachnik, N.M.; Uphues, T.; Uiberacker, M.; Yakovlev, V.; Krausz, F.; Drescher, M.; Kleineberg, U.; Heinzmann, U. *Appl. Opt.* **2006**, *45*, 4147–4156.

- [86] Goulielmakis, E.; Schultze, E.M.; Hofstetter, M.; Yakovlev, V.S.; Gagnon, J.; Uiberacker, M.; Aquila, A.L.; Gullikson, E.M.; Attwood, D.T.; Kienberger, R.; Krausz, F.; Kleineberg, U. *Science* **2008**, *320*, 1614–1617.
- [87] Paul, A.; Bartels, R.A.; Tobey, R.; Green, H.; Weiman, S.; Christov, I.P.; Murnane, M.M.; Kapteyn, H.C.; Backus, S. *Nature* **2003**, *421*, 51–54.
- [88] Takahashi, E.J.; Kanai, T.; Ishikawa, K.L.; Nabekawa, Y.; Midorikawa, K. *Phys. Rev. Lett.* **2007**, *99*, 053904.
- [89] Thaur, C.; Quéré, F.; Geindre, J.-P.; Levy, A.; Ceccotti, T.; Monot, P.; Bougeard, M.; Réau, F.; D'Oliveira, P.; Audebert, P.; Marjoribanks, R.; Marin, Ph. *Nat. Phys.* **2007**, *3*, 424–429.
- [90] Tsakiris, G.D.; Eidmann, K.; Meyer-ter-Vehn, J.; Krausz, F. *New J. Phys.* **2006**, *8*, 19–39.
- [91] Gordienko, S.; Pukhov, A.; Shorokhov, O.; Baeva, T. *Phys. Rev. Lett.* **2004**, *93*, 115002.
- [92] Baeva, T.; Gordienko, S.; Pukhov, A. *Phys. Rev. E* **2006**, *74*, 046404.
- [93] Dromey, B.; Zepf, M.; Gopal, A.; Lancaster, K.; Wei, M.S.; Krushelnick, K.; Tatarakis, M.; Vakakis, N.; Moustazis, S.; Kodama, R.; Tampo, M.; Stoekl, C.; Clarke, R.; Habara, H.; Neely, D.; Karsch, S.; Norreys, P. *Nat. Phys.* **2006**, *2*, 456–459.
- [94] Dromey, B.; Kar, S.; Bellei, C.; Carroll, D.C.; Clarke, R.J.; Green, J.S.; Kneip, S.; Markey, K.; Nagel, S.R.; Simpson, P.T.; Willingale, L.; McKenna, P.; Neely, D.; Najmudin, Z.; Krushelnick, K.; Norreys, P.A.; Zepf, M. *Phys. Rev. Lett.* **2007**, *99*, 085001.
- [95] Yudin, G.L.; Ivanov, M.Y. *Phys. Rev. A* **2001**, *63*, 033404.
- [96] Serebryannikov, E.E.; Verhoef, A.J.; Mitrofanov, A.; Baltuška, A.; Zheltikov, A.M. *Phys. Rev. A* **2009**, *80*, 053809.
- [97] Popov, V.S. *Phys. Usp.* **2004**, *47*, 855–885.
- [98] Schultze, M.; Goulielmakis, E.; Uiberacker, M.; Hofstetter, M.; Kim, J.; Kim, D.; Krausz, F.; Kleineberg, U. *New J. Phys.* **2007**, *9*, 243–253.
- [99] Mauritsson, J.; Johnsson, P.; Mansten, E.; Swoboda, M.; Ruchin, T.; L'Huillier, A.; Schafer, K.J. *Phys. Rev. Lett.* **2008**, *100*, 073003.
- [100] Gallagher, T.F. *Phys. Rev. Lett.* **1988**, *61*, 2304–2307.
- [101] Itatani, J.; Quéré, F.; Yudin, G.L.; Ivanov, M.Yu.; Krausz, F.; Corkum, P.B. *Phys. Rev. Lett.* **2002**, *88*, 173903.
- [102] Kienberger, R.; Hentschel, M.; Uiberacker, M.; Spielmann, Ch.; Kitzler, M.; Scrinzi, A.; Wieland, M.; Westerwalbesloh, Th.; Kleinberg, U.; Heinzmann, U.; Drescher, M.; Krausz, F. *Science* **2002**, *297*, 1144–1148.
- [103] Johnsson, P.; López-Martens, R.; Kazamias, S.; Mauritsson, J.; Valentin, C.; Remetter, T.; Varjú, K.; Gaarde, M.B.; Mairesse, Y.; Wabnitz, H.; Salières, P.; Balcou, Ph.; Schafer, K.; L'Huillier, A. *Phys. Rev. Lett.* **2005**, *95*, 013001.
- [104] Cederbaum, L.S.; Zobeley, J. *Chem. Phys. Lett.* **1999**, *307*, 205–210.
- [105] Breidbach, J.; Cederbaum, L.S. *J. Chem. Phys.* **2003**, *118*, 3983–3996.
- [106] Hennig, H.; Breidbach, J.; Cederbaum, L.S. *J. Chem. Phys.* **2005**, *122*, 134104.
- [107] Kuleff, A.I.; Breidbach, J.; Cederbaum, L.S. *J. Chem. Phys.* **2005**, *123*, 044111.
- [108] Breidbach, J.; Cederbaum, L.S. *Phys. Rev. Lett.* **2005**, *94*, 033901.
- [109] Remacle, F.; Levine, R.D. *Proc. Natl. Am. Sci. USA* **2006**, *103*, 6793–6798.
- [110] Remacle, F.; Levine, R.D. *Z. Phys. Chem.* **2007**, *221*, 647–661.
- [111] Weinkauff, R.; Schanen, P.; Metsala, A.; Schlag, E.W.; Bürgle, M.; Kessler, H. *J. Phys. Chem.* **1996**, *100*, 18567–18585.
- [112] Weinkauff, R.; Schlag, E.W.; Martinez, T.J.; Levine, R.D. *J. Phys. Chem. A* **1997**, *101*, 7702–7710.
- [113] Ikeura-Sekiguchi, H.; Sekiguchi, T. *Phys. Rev. Lett.* **2007**, *99*, 228102.
- [114] Brühwiler, P.A.; Karis, O.; Mårtensson, N. *Rev. Mod. Phys.* **2002**, *74*, 703–740.
- [115] Krause, M.O.; Oliver, J.H. *J. Phys. Chem. Ref. Data* **1979**, *8*, 329–338.
- [116] Rosenzweig, J.B.; Alesini, D.; Andonian, G.; Boscolo, M.; Dunning, M.; Faillace, L.; Ferrario, M.; Fukusawa, A.; Giannessi, L.; Hemsing, E.; Marcus, G.; Marinelli, A.; Musumeci, P.; O'Shea, B.; Palumbo, L.; Pellegrini, C.; Pettrillo, V.; Reiche, S.; Ronsivalle, C.; Spataro, B.; Vaccarezza, C. *Nucl. Instrum. Meth. A* **2008**, *593*, 39–44.
- [117] Reiche, S.; Musumeci, P.; Pellegrini, C.; Resenzweig, J.B. *Nucl. Instrum. Meth. A* **2008**, *593*, 45–48.
- [118] Stockman, M.I.; Kling, M.F.; Kleinberg, U.; Krausz, F. *Nat. Photon.* **2007**, *1*, 539–544.
- [119] Bauer, M. *J. Phys. D: Appl. Phys.* **2005**, *38*, R253–R267.
- [120] Miaja-Avila, L.; Lei, C.; Aeschlimann, M.; Gland, J.L.; Murnane, M.M.; Kapteyn, H.C.; Saathoff, G. *Phys. Rev. Lett.* **2006**, *97*, 113604.
- [121] Stapelfeldt, H.; Seidemann, T. *Rev. Mod. Phys.* **2003**, *75*, 543.
- [122] Torres, R.; de Nalda, R.; Marangos, J.P. *Phys. Rev. A* **2005**, *72*, 023420.
- [123] Friedrich, B.; Herschbach, D. *Phys. Rev. Lett.* **1995**, *74*, 4623–4626.
- [124] Underwood, J.G.; Sussman, B.J.; Stolow, A. *Phys. Rev. Lett.* **2005**, *94*, 143002.
- [125] Corkum, P.B. *Phys. Rev. Lett.* **1993**, *71*, 1994.
- [126] Lein, M.; Marangos, J.P.; Knight, P.L. *Phys. Rev. A* **2002**, *66*, 051404.
- [127] Spanner, M.; Smirnova, O.; Corkum, P.B.; Ivanov, M.Yu. *J. Phys. B* **2004**, *37*, L243–L250.
- [128] Yurchenko, S.N.; Patchkovskii, S.; Litvinyuk, I.V.; Corkum, P.B.; Yudin, G.L. *Phys. Rev. Lett.* **2004**, *93*, 223003.
- [129] Hu, S.X.; Collins, L.A. *Phys. Rev. Lett.* **2005**, *94*, 073004.
- [130] Velotta, R.; Hay, N.; Mason, M.B.; Castillejo, M.; Marangos, J.P. *Phys. Rev. Lett.* **2001**, *87*, 183901.
- [131] Lein, M.; Hay, N.; Velotta, R.; Marangos, J.P.; Knight, P.L. *Phys. Rev. Lett.* **2002**, *88*, 183903.

- [132] Lein, M.; Hay, N.; Velotta, R.; Marangos, J.P.; Knight, P.L. *Phys. Rev. A* **2002**, *66*, 023805.
- [133] Kanai, T.; Minemoto, S.; Sakai, H. *Nature* **2005**, *435*, 470–474.
- [134] Vozzi, C.; Calegari, F.; Benedetti, E.; Caumes, J.P.; Sansone, G.; Stagira, S.; Nisoli, M.; Torres, R.; Heesel, E.; Kajumba, N.; Marangos, J.P.; Altucci, C.; Velotta, R. *Phys. Rev. Lett.* **2005**, *95*, 153902.
- [135] Burnett, K.; Reed, V.C.; Cooper, J.; Knight, P.L. *Phys. Rev. A* **1992**, *45*, 3347–3349.
- [136] Lewenstein, M.; Balcou, P.; Ivanov, M.Y.; L’Huillier, A.; Corkum, P.B. *Phys. Rev. A* **1994**, *49*, 2117–2132.
- [137] Bandrauk, A.D.; Yu, H. *Phys. Rev. A* **1999**, *59*, 539–548.
- [138] Lappas, D.G.; Marangos, J.P. *J. Phys. B* **2000**, *33*, 4679–4689.
- [139] Torres, R.; Kajumba, N.; Underwood, J.G.; Robinson, J.S.; Baker, S.; Tisch, J.W.G.; de Nalda, R.; Bryan, W.A.; Velotta, R.; Altucci, C.; Turcu, I.C.E.; Marangos, J.P. *Phys. Rev. Lett.* **2007**, *98*, 203007.
- [140] Antoine, P.; L’Huillier, A.; Lewenstein, M. *Phys. Rev. Lett.* **1996**, *77*, 1234–1237.
- [141] Lein, M. *Phys. Rev. Lett.* **2005**, *94*, 053004.